



**HAL**  
open science

# Effective global mixing of the highly siderophile elements into Earth's mantle inferred from oceanic abyssal peridotites

Marine Paquet, James M.D. Day, Diana B Brown, Christopher L Waters

► **To cite this version:**

Marine Paquet, James M.D. Day, Diana B Brown, Christopher L Waters. Effective global mixing of the highly siderophile elements into Earth's mantle inferred from oceanic abyssal peridotites. *Geochimica et Cosmochimica Acta*, 2021, 316, pp.347 - 362. 10.1016/j.gca.2021.09.033 . hal-04092171

**HAL Id: hal-04092171**

**<https://hal.science/hal-04092171>**

Submitted on 15 May 2023

**HAL** is a multi-disciplinary open access archive for the deposit and dissemination of scientific research documents, whether they are published or not. The documents may come from teaching and research institutions in France or abroad, or from public or private research centers.

L'archive ouverte pluridisciplinaire **HAL**, est destinée au dépôt et à la diffusion de documents scientifiques de niveau recherche, publiés ou non, émanant des établissements d'enseignement et de recherche français ou étrangers, des laboratoires publics ou privés.



Distributed under a Creative Commons Attribution - NonCommercial - NoDerivatives 4.0 International License

1 Effective global mixing of the highly siderophile elements into  
2 Earth's mantle inferred from oceanic abyssal peridotites

3

4 Marine Paquet<sup>1,2</sup>, James M.D. Day<sup>1</sup>, Diana B. Brown<sup>1</sup>, Christopher L. Waters<sup>1</sup>

5

6 <sup>1</sup>*Scripps Institution of Oceanography, University of California San Diego, La Jolla, CA 92093,*

7 *USA ([mpaquet@ucsd.edu](mailto:mpaquet@ucsd.edu), [jmdday@ucsd.edu](mailto:jmdday@ucsd.edu))*

8 <sup>2</sup>*Institut de Physique du Globe de Paris, UMR 7154 CNRS, Université de Paris, 1 rue Jussieu,*

9 *75238 Paris, France*

10

11

12 **Manuscript Statistics**

13 Abstract: 407 words

14 Main Text: 6689 words

15 Figures: 8 (+6 supplementary figures)

16 Tables: 1 (+7 supplementary tables)

17

18

19

20

21

22

23 Keywords: Oceanic mantle; peridotite; highly siderophile elements; Os isotopes; late accretion;

24 mantle convection; heterogeneity

25

26 **ABSTRACT**

27 Late accretion occurred through addition of massive impactors to Earth, leading to potential  
28 heterogeneities in the distribution of highly siderophile elements (HSE: Os, Ir, Ru, Pt, Pd, Re)  
29 within the mantle. Abyssal peridotites sample the present-day convecting mantle, which make  
30 them useful for examining the distribution of the HSE within the mantle. Here we report new HSE  
31 abundance data and  $^{187}\text{Os}/^{188}\text{Os}$  ratios, in conjunction with mineral chemistry and bulk rock major-  
32 and trace-element compositions for abyssal peridotites from the fast-spreading Pacific Antarctic  
33 Ridge (PAR) and East Pacific Rise (Hess Deep), and for slow to intermediate spreading ridges  
34 from the Southwest Indian Ridge, Central Indian Ridge and Mid Atlantic Ridge. These analyses  
35 expand the global abyssal peridotite Os isotope and HSE database, enabling evaluation of potential  
36 variations with spreading rate, from ultraslow (<20 mm, full spreading rate) to fast (135-150  
37 mm/yr). Accounting for likely effects from seawater modification and serpentinization, the Pacific  
38 data reveals heterogeneous and sometimes significant melt depletion for PAR (3-23% melt  
39 depletion;  $^{187}\text{Os}/^{188}\text{Os}$  from 0.1189 to 0.1336, average =  $0.1267 \pm 0.0065$ ; 2SD) and Hess Deep  
40 abyssal peridotites (15-20% melt depletion;  $0.1247 \pm 0.0027$ ). Abyssal peridotites from fast to  
41 intermediate spreading ridges reveal no systematic differences in the distribution and behavior of  
42 the HSE or Os isotopes, or in degrees of melt depletion, compared with slow to ultraslow spreading  
43 ridges. These observations arise despite significant differences in melt generation processes at mid-  
44 ocean ridges suggesting that the effects of ancient melt depletion are more profound on HSE  
45 compositions in abyssal peridotites than modern melting beneath ridges. Using global abyssal  
46 peridotites with  $\text{Al}_2\text{O}_3$  content > 2 wt.%, the average composition of the primitive mantle is 0.3  
47 ppb Re, 4.9 ppb Pd, 7.1 ppb Pt, 7.2 ppb Ru, 3.8 ppb Ir and Os, showing no Pd/Ir, but a positive  
48 Ru/Ir anomaly, relative to chondrites. There is ~50% variation of the HSE abundances in the  
49 oceanic mantle, with much of this variation being observed at small length scales (<1 km) and due  
50 entirely to both modern and more ancient partial melting effects. Consequently, any significant  
51 HSE heterogeneities formed during late accretion or early Earth differentiation processes are no  
52 longer recognizable in the mantle sampled within ocean basins, implying generally efficient  
53 mixing of Earth's mantle for these elements. By contrast, relatively ancient heterogeneity in Os  
54 and other radiogenic isotopes has been effectively preserved in the convecting mantle over the last  
55 ~2 Ga, through recycling processes and through preservation and isolation of melt-depleted  
56 refractory residues.

## 57 1. INTRODUCTION

58 The highly siderophile elements (HSE: Os, Ir, Ru, Pt, Rh, Pd, Re, Au) are key geochemical  
59 tools with which to investigate terrestrial accretion and differentiation processes. The HSE are  
60 generally compatible during partial melting and are characterized by elevated metal-silicate  
61 partition coefficients at mantle pressures ( $> 10^4$ ; e.g., O'Neill et al., 1995; Holzheid et al., 2000;  
62 Ertel et al., 2001; Brenan and McDonough, 2009; Brenan et al., 2016; Suer et al., 2021 and  
63 references therein). Assuming such high partition coefficients, Earth's core and mantle are not in  
64 equilibrium for the HSE, and the mantle has abundances of these elements only  $\sim 150$  times less  
65 abundant than in chondrites; some three orders of magnitude higher than expected (Morgan, 1986;  
66 Snow and Schmidt, 1998; Morgan et al., 2001; Becker et al., 2006; Fischer-Gödde et al., 2011;  
67 Day et al., 2016a; 2017a).

68  
69 Three main hypotheses have been suggested to explain this discrepancy: (1) the "late  
70 accretion" or "late veneer" hypothesis where addition of "chondritic" impactors occurred after the  
71 major phase(s) of core formation (e.g., Turekian and Clark, 1969; Kimura et al., 1974; Chou, 1978;  
72 Jagoutz et al., 1979; Wänke, 1981; Meisel et al., 1996); (2) mixing or inefficient separation of  
73 differentiated outer-core material back into the mantle shortly after core separation (Jones &  
74 Drake, 1986; Snow & Schmidt, 1998), or; (3) lower metal-silicate partition coefficients at higher  
75 pressures and temperatures (HP-HT; e.g., Ringwood, 1977; Murthy, 1991). The late accretion  
76 model is generally the most popular given its ability to explain both the broadly chondritic  
77  $^{187}\text{Os}/^{188}\text{Os}$  as well as the elevated absolute abundances of the HSE that are in chondritic  
78 proportions within the bulk silicate Earth (BSE), requiring between  $\sim 0.5$  and 0.8 wt.% addition of  
79 mass to Earth (Becker et al., 2006; Day et al., 2016a).

80

81           An outstanding question that remains, however, is how evenly distributed the HSE are  
82 within the present-day convecting mantle. Late accretion likely occurred through addition of  
83 massive impactors (Bottke et al., 2010), leading to the possibility of heterogeneous distribution of  
84 the HSE within Earth's mantle following late accretionary impacts, and enhanced deposition of  
85 impactor material within the mantle, perhaps at hemispheric scales, or at the scale of thousands of  
86 kilometers. For example, it has been demonstrated that metal-silicate equilibration differs  
87 depending on the target latitude of the impactor due to the influence of the planetary rotation on  
88 the mixing and settling history, which may generate chemical heterogeneities (e.g., HSE) and  
89 isotopic anomalies (e.g.,  $^{182}\text{W}$  anomalies) (Maas et al., 2021). For smaller planetary bodies, such  
90 as the probable asteroidal source of eucrite and diogenite meteorites, 4-Vesta, it has been proposed  
91 that the inferred patchy distribution of the HSE reflects regional rather than global late accretion  
92 effects shortly after planet formation (Day et al., 2012). In contrast, while Earth may have  
93 originally had a more heterogeneous distribution of the HSE within the mantle, compositional  
94 variations in mantle materials at the present-day are seemingly more consistent with homogeneous  
95 distributions through prolonged melting and/or solid-state convection. The evidence from mantle  
96 peridotites preserved in ophiolites is that there is more limited heterogeneity at >km length scales  
97 than at the scale of meters or less (e.g., O'Driscoll et al., 2012; Snortum & Day, 2020; Haller et  
98 al., 2021). Arguably, however, the ideal test of HSE homogeneity in Earth's mantle comes from  
99 the study of oceanic abyssal peridotites. Abyssal peridotites are samples of Earth's present-day  
100 convecting mantle sampled within ocean basins, so provide a snap-shot of the degree of present-  
101 day HSE homogeneity within the mantle.

102

103           Prior attempts to estimate the HSE composition of Earth's mantle have assumed relative  
104 initial homogeneity to attain a BSE composition (equivalent to primitive mantle [PM] and referred  
105 to as primitive upper mantle [PUM] by Becker et al., 2006), with workers utilizing a range of  
106 mantle rock types, including ultramafic massifs and ophiolites (e.g., Becker et al., 2006; Zhang et  
107 al., 2020), as well as using abyssal peridotites (e.g., Becker et al., 2006; Day et al., 2017a). These  
108 approaches for determining the absolute and relative abundances of the HSE in the bulk silicate  
109 Earth, and the extent of heterogeneity have drawbacks. For example, utilizing massif compositions  
110 requires effective subtraction of the effects of sometimes complex melt refertilization processes  
111 (e.g., Marchesi et al., 2014; Becker and Dale, 2016; Lorand and Luguet, 2016). Abyssal peridotites  
112 represent residues of ancient and modern depletion events (2% to >16%), which occurred > 0.5  
113 Ga ago for some samples (e.g., Brandon et al., 2000; Harvey et al., 2006; Liu et al., 2008; Lassiter  
114 et al., 2014; Day et al., 2017a). Complications with these samples are that melt refertilization (e.g.,  
115 Niu, 2004; Warren, 2016; Reisberg, 2021) and serpentinization or secondary alteration (e.g., Snow  
116 and Dick, 1995; Snow and Reisberg, 1995; Malvoisin, 2015) processes can affect their  
117 compositions. Furthermore, abyssal peridotites are difficult to sample, being either dredged or  
118 drilled typically from deep water locations (>3 km) and relatively rare exposures on the ocean  
119 floor, such that global coverage has hitherto not been obtained.

120

121           Currently, HSE and Os isotope data for abyssal peridotites are mainly from ultraslow to  
122 slow spreading ridges (e.g., Gakkal Ridge, Southwest Indian Ridge, Central Indian Ridge, Mid-  
123 Atlantic Ridge; Martin, 1991; Roy-Barman & Allègre, 1994; Snow & Reisberg, 1995; Snow &  
124 Schmidt 1998; Brandon et al., 2000; Luguet et al., 2001; 2003; Standish et al, 2002; Alard et al.,  
125 2005; Harvey et al., 2006; Sichel et al., 2008; Liu et al., 2008; 2009; Lassiter et al., 2014; Day et

126 al., 2017a). More limited data are available on the HSE abundances and Os isotopic composition  
127 of mantle beneath intermediate and fast spreading centers (Roy-Barman and Allègre, 1994; Snow  
128 and Schmidt, 1998; Rehkämper et al., 1999). Here we report new bulk rock  $^{187}\text{Os}/^{188}\text{Os}$  and HSE  
129 abundance data for abyssal peridotites from the Pacific Ocean (Hess Deep along the East Pacific  
130 Rise (EPR) and from the Udintsev Fracture Zone (UFZ) along the Pacific Antarctic Ridge (PAR)).  
131 We compare these data with those obtained for abyssal peridotites from ultraslow to slow  
132 spreading ridges (e.g., Gakkel Ridge, Southwest Indian Ridge (SWIR), Central Indian Ridge  
133 (CIR), Mid-Atlantic Ridge (MAR)). Additionally, new bulk rock major and trace element  
134 abundances and mineral chemistry are reported for some samples to examine the relationship to  
135 spreading rate and melt depletion in abyssal peridotites, and to assess heterogeneity of mantle  
136 composition in terms of HSE abundances and Os isotope ratios and the implications this might  
137 have for mantle geodynamics.

138

## 139 **2. SAMPLES AND METHODS**

### 140 *2.1 Samples*

141 Dredged abyssal peridotites were analyzed from the fast-spreading East Pacific Rise (EPR),  
142 at Hess Deep (denoted AII) from cruise 125, leg 6, aboard the RV Atlantis II in May 1990. Dredged  
143 abyssal peridotites were also analyzed from the Pacific Antarctic Ridge (PAR), along two different  
144 locations of the Udintsev ridge, denoted as WEST03-MV12 and WEST03-MV13, from the  
145 WESTWARD (WEST03MV) cruise aboard the RV Melville in February 1994. Details for this  
146 cruise are reported in Castillo et al. (1998) and Niu (2004). New data are also reported for abyssal  
147 peridotites from slower spreading rates (Mid Atlantic Ridge, Central Indian Ridge and Southwest  
148 Indian Ridge) from the 1968 CIRCE cruise (Circe97) aboard the RV Argo, the 1970 ANTIPODE

149 cruise (ANTP) aboard the RV Melville, 1984 Protea Cruise (Prot05) aboard the RV Melville, the  
150 1990 PLUME cruise (PLUM05) aboard the RV Thomas Washington, and the 2007 KNOX11RR  
151 cruise aboard the RV Roger Revelle. Sample locations are reported in Figure 1 and Table 1.

152

## 153 ***2.2 Mineral compositions***

154 Major- and minor-element mineral compositions were obtained from polished mounts  
155 containing olivine, pyroxene and spinel, and as polished thick sections for Hess Deep and PAR  
156 samples, using a JEOL JXA-8230 electron probe micro analyzer (EPMA) at the University of  
157 Colorado, USA (Department of Geological Sciences). Analyses were made with an accelerating  
158 potential of 15 keV and a beam size of 5  $\mu\text{m}$ . Beam currents were 30 nA for olivine and pyroxene  
159 and 20 nA for spinel. Both natural and synthetic standards were used to calibrate the EMP and  
160 were measured throughout analytical sessions to ensure data quality. Background and peak  
161 counting times used were 20-30 s and standard PAP correction procedures were used. Detection  
162 limits were  $\leq 0.02$  wt.% for Si, Al, Mg, Ca, Na, K and P and  $< 0.04$  wt.% for Fe, Ti, Mn, V, Ni  
163 and Cr.

164

## 165 ***2.3 Bulk rock major and trace element abundance analyses***

166 Major element compositions were measured by X-ray fluorescence (XRF) at Franklin and  
167 Marshall College using a PW 2404 PANalytical XRF vacuum spectrometer following the protocol  
168 described in Day et al. (2017a) and references therein. Repeated measurements of basaltic  
169 reference material BHVO-2 allow estimations of precision and accuracy, with long-term  
170 reproducibility of 0.1% for  $\text{SiO}_2$ ,  $\text{Al}_2\text{O}_3$ ,  $\text{Fe}_2\text{O}_{3\text{T}}$ , MgO and CaO, 0.2% for  $\text{TiO}_2$ , MnO and  $\text{Na}_2\text{O}$ ,  
171 and 0.3% for  $\text{P}_2\text{O}_5$  (Table S1).



172

173 Trace elements analyses were performed on 100 mg of homogenized bulk rock powder  
174 using a *Thermo Scientific* iCAP Qc ICP-MS at the Scripps Isotope Geochemistry Laboratory  
175 (SIGL, University of California San Diego), following the method outlined in Day et al. (2014).  
176 Samples were analyzed with several replicates of powdered peridotites HAZ-01 and PLUM05-  
177 49, as well as BHVO-2, BCR-2 and BIR-1a, basaltic reference materials, used as standards to  
178 confirm accuracy, with reproducibility on most of trace element abundances better than 10%  
179 (Table S2).

180

181

#### ***2.4 Highly siderophile elements and Os isotopic compositions***

182

183

184

185

186

187

188

189

190

191

192

193

194

Osmium isotope and HSE abundance analyses were performed at the SIGL on ~900 mg of homogenized powder from a larger powder aliquot. The samples were precisely weighed and digested in sealed 20 cm borosilicate Carius tubes using a mixture of multiply Teflon distilled 12M HCl (4 mL) and “purged” 15.7M HNO<sub>3</sub> (7 mL; expunged of Os using H<sub>2</sub>O<sub>2</sub>), with isotopically enriched multi-element spikes (<sup>99</sup>Ru, <sup>106</sup>Pd, <sup>185</sup>Re, <sup>190</sup>Os, <sup>191</sup>Ir, <sup>194</sup>Pt). Digestions lasted 72h hours in an oven at a maximum temperature of 250°C. Osmium was purified by extracting CCl<sub>4</sub> three times from the HCl/HNO<sub>3</sub>, spike and sample mixture and then back extracting the Os from the CCl<sub>4</sub> using HBr (Cohen and Waters, 1996), with further purification by micro-distillation (Birck et al., 1997). The other HSE (Re, Pd, Pt, Ru, Ir) were recovered and purified from the residual solutions using anion exchange column chemistry (e.g., Day et al., 2016b).

Acquisition of Os isotopic compositions were performed on a *Thermo Scientific* Triton thermal ionization mass spectrometer in negative ion mode, with HSE abundances calculated from

195 isotopic ratios of Ir, Ru, Pt, Pd and Re measured using a *Thermo Scientific* iCaP Qc ICP-MS  
196 coupled to a *Cetac Aridus II* desolvating nebulizer. Osmium data were appropriately oxide-,  
197 fractionation-, spike- and blank corrected. Precision for  $^{187}\text{Os}/^{188}\text{Os}$ , determined by repeated  
198 measurements of 35 to 70 pg loads of the UMCP Johnson-Matthey standard, was better than  $\pm 0.2$   
199 % (2SD;  $0.11382 \pm 0.00012$ ;  $n = 10$ ). These standard load sizes were smaller than unknown  
200 samples, which had  $>1$  ng Os, and that typically ran with signal sizes of 200 K Cps on the largest  
201 mass isotope, with stable signals similar to the standards. Rhenium, Pd, Pt, Ir and Ru isotopic ratios  
202 were corrected for mass fractionation using the deviation of the standard average run on the day  
203 over the natural ratio of the element. External reproducibility on HSE analyses was better than  
204 0.5% for 5 ppb solutions and all reported values are blank corrected. Peridotite standard reference  
205 materials (MUH-1, HARZ-01) run during the period of the analytical campaign in the SIGL are  
206 reported in Day et al. (2016a) and Snortum & Day (2020) and show good reproducibility and  
207 accuracy compared with literature data (e.g., Meisel & Horan, 2016). The total procedural blanks  
208 ( $n = 4$ ) run with the samples had  $^{187}\text{Os}/^{188}\text{Os} = 0.209 \pm 0.090$ , with quantities (in pg) of 0.8 [Re], 7  
209 [Pd], 22 [Pt], 15 [Ru], 3 [Ir] and 0.8 [Os]. These blanks resulted in negligible corrections to samples  
210 ( $<1\%$  in most cases, Table S3).

211

## 212 **3 RESULTS**

### 213 ***3.1 Sample descriptions and mineral chemistry***

214 Spinel grains in the PAR abyssal peridotites from WEST03MV-12 and WEST03MV-13 span  
215 a Mg# range of 58.4 to 70.6 and 68.7 to 72.7, and a Cr# range of 28.7 to 49.6 and 19.1 to 24.9,  
216 respectively, similar to plagioclase-free peridotites (e.g., SWIR peridotites, Seyler et al., 2003;  
217 global abyssal peridotite database, Warren, 2016). Spinel grains in Hess Deep (EPR) samples have

218 Mg# between 45.6 and 60.0, and Cr# between 47.3 and 52.0 (e.g., comparable to plagioclase-  
219 lherzolites from the SWIR; Paquet et al., 2016) (Figure S1a).

220

221 Forsterite contents in olivine grains range between 89.7 and 90.7, and between 90.0 and 90.6  
222 in WEST03MV-12 and WEST03MV-13 samples, respectively (Table S4). Orthopyroxenes and  
223 clinopyroxenes in PAR samples have similar compositions: between  $Wo_{0.01-0.07}En_{0.84-0.89}Fs_{0.08-0.10}$   
224 and  $Wo_{0.32-0.49}En_{0.47-0.62}Fs_{0.05-0.07}$  for WEST03MV-12 peridotites, and between  $Wo_{0.01-0.11}En_{0.81-}$   
225  $0.89}Fs_{0.09-0.10}$  and  $Wo_{0.35-0.49}En_{0.46-0.59}Fs_{0.04-0.06}$  for the WEST03MV-13 peridotites (Figure S1b).  
226 WEST03MV-12 and WEST03MV-13 peridotites have  $Cr_2O_3$  contents that range from 0.66 to 1.08  
227 wt.% and from 0.43 to 0.96 wt.% in orthopyroxenes, and from 0.95 to 1.43 wt.% and from 0.56 to  
228 1.32 wt.% in clinopyroxenes, respectively (Table S4). These values are within the compositions  
229 of abyssal peridotites from the global ridge system (e.g., Warren, 2016). Olivine, orthopyroxene  
230 and clinopyroxene grains in the EPR samples were not fresh enough to conduct analyses on.

231

### 232 ***3.2 Bulk rock major and trace element abundances***

233 Hess Deep abyssal peridotites tend to have lower anhydrous-corrected  $Al_2O_3$ ,  $TiO_2$  and  
234  $CaO$ , and higher  $MgO$  contents than to those from the Pacific Antarctic Ridge (Figure 2, Table  
235 S5). The WEST03MV-13 peridotites generally have lower  $Al_2O_3$ ,  $TiO_2$  and  $CaO$  (and  $Fe_2O_{3T}$  to a  
236 lesser extent) at a given  $MgO$  than the WEST03MV-12 peridotites suggesting heterogeneity at the  
237 scale of the fracture zone that they were dredged from. All these peridotites show a positive  
238 correlation between  $Al_2O_3$  and  $CaO$ , with Hess Deep peridotites being both tightly grouped in  
239 terms of composition and having the most refractory (lowest)  $Al_2O_3$  and  $CaO$  contents. Overall,  
240 the Pacific abyssal peridotites overlap the trend defined by abyssal peridotites from ridges with

241 slower spreading rates (Day et al., 2017a).

242

243 Abyssal peridotites from the UFZ along the PAR are characterized by having subchondritic  
244 rare earth element (REE) abundances, and show pronounced LREE-depleted patterns, which are  
245 similar to abyssal peridotites from the Mid-Atlantic Ridge, and some samples from the SWIR and  
246 Gakkel ridge (Day et al., 2017a) (Figures 3, S2 and Table S6). Samples from the West region span  
247 a larger range of REE abundances. Abyssal peridotites from Hess Deep are depleted in the heavy  
248 REE, with REE patterns slightly depleted in the light REE (LREE) relative to the HREE, and  
249 strong positive anomalies for Eu, suggesting melt impregnation and plagioclase crystallization. A  
250 few samples from the PAR, SWIR and CIR also show negative Ce anomalies. Overall, abyssal  
251 peridotites from the WEST03MV-13 dredge tend to have higher Nb and Ta abundances, and lower  
252 Zr and Hf abundances than those from the WEST03MV-12 dredge. Abyssal peridotites from Hess  
253 Deep exhibit depleted patterns in Rb, Ba, Nb, Ta, Zr and Hf compared to other Pacific peridotites.  
254 Overall, incompatible trace element (ITE) and REE abundances for abyssal peridotites from the  
255 SWIR are in good agreement with data reported in previous studies (e.g., Day et al, 2017a) (Figures  
256 3, S2 and Table S6).

257

258 Abyssal peridotites from the CIR reported in this study show more depleted patterns in the  
259 REE, and for the ITE in general with lower Nb contents (and slightly higher Ta abundances), than  
260 previously reported samples (e.g., Day et al., 2017a). PLUM05 abyssal peridotite samples from  
261 the MAR have HREE similar to those from the same ocean basin in the literature but are more  
262 enriched in the LREE and have more pronounced positive Eu anomalies. They also exhibit higher  
263 contents in Rb, Ba, Nb and Ta, but lower Zr and Hf abundances than those from Day et al. (2017a).

264 Most abyssal peridotites show elevated concentrations in fluid mobile elements such as U and Sr  
265 which are enriched in seawater (Figure S2).

266

### 267 ***3.3 Highly siderophile element abundances and Os isotopic compositions***

268 Bulk rock Re-Os isotope and highly siderophile-element (HSE: Re, Pd, Pt, Ru, Ir, Os)  
269 abundance measurements for Pacific abyssal peridotites and some Southwest Indian Ridge and  
270 Central Indian Ridge peridotites are reported in Table 1. PAR samples from the WEST03MV-13  
271 dredge have BSE-like HSE patterns with variable rhenium depletion, whereas samples from the  
272 WEST03MV-12 dredge have more variable Re, Pd and Pt abundances (Figure 4), similar to those  
273 reported previously (Roy-Barman and Allègre, 1994; Snow and Schmidt, 1998; Rehkämper et al.,  
274 1999). Two of the Hess Deep samples have patterns that are akin to BSE, while the other samples  
275 show variable degrees of rhenium depletion relative to BSE. WEST03MV-12 and WEST03MV-  
276 13 abyssal peridotites have average Pd/Ir ratios of  $1.4 \pm 0.6$  and  $1.4 \pm 1.1$  (2 SD), and average  
277 Ru/Ir ratios of  $1.7 \pm 0.2$  and  $1.8 \pm 0.4$  respectively (Figure 5). Hess Deep samples show average  
278 ratios slightly higher but within uncertainties at  $1.9 \pm 1.1$  and  $2.0 \pm 0.6$  for Pd/Ir and Ru/Ir ratios,  
279 respectively. Moreover, HSE patterns for the Pacific abyssal peridotites are like those from the  
280 Mid-Atlantic Ridge, and some of the abyssal peridotites from the Southwest Indian Ridge (Day et  
281 al., 2017a and references therein).

282

283 Pacific Antarctic Ridge peridotites show similar ranges and averages in  $^{187}\text{Os}/^{188}\text{Os}$   
284 (WEST03MV-12:  $0.1264 \pm 0.0054$ ; WEST03MV-13:  $0.1272 \pm 0.0082$ ; all uncertainties are 2 SD),  
285 and are slightly more radiogenic, on average, than the samples from Hess Deep ( $0.1247 \pm 0.0030$ )  
286 (Figure 6), with an average value of  $0.1264 \pm 0.0063$  for all Pacific abyssal peridotites from this

287 study. Using the Os abundances in the samples to calculate a weighted mean, we obtained a  
288  $^{187}\text{Os}/^{188}\text{Os}$  ratio of 0.1263. These new data overlap the trend defined by abyssal peridotites from  
289 slower spreading ridges (Snow & Schmidt, 1998; Rehkämper et al., 1999; Luguët et al., 2001; Liu  
290 et al., 2009; Lassiter et al., 2014; Day et al., 2017a), but are generally more radiogenic than mantle  
291 peridotites obtained from Pacific Ocean Islands (Snortum et al., 2019), which offer an alternate  
292 view of the Pacific oceanic mantle lithosphere.

293

## 294 **4 DISCUSSION**

### 295 *4.1 Alteration and melt infiltration*

296 Most abyssal peridotites have experienced serpentinization (<400 °C) and/or sea-floor  
297 weathering (~0°C) under both oxidizing and reducing conditions (e.g., Snow & Dick, 1995; Bach  
298 et al., 2004; Paulick et al., 2006; Klein et al., 2013; Malvoisin, 2015). Samples in this study exhibit  
299 evidence for secondary alteration, manifested as loss on ignition (LOI) values of between ~5 and  
300 17%, reflecting the presence of serpentine and other alteration minerals. As noted for abyssal  
301 peridotites from a range of spreading ridge environments (Niu, 2004; Harvey et al., 2006; Day et  
302 al., 2017a), elevated concentrations of fluid mobile elements, occur in many of the samples,  
303 consistent with modification by interaction with seawater (e.g., U, Sr, K, P, Na, LREE; e.g., Frisby  
304 et al., 2016). However, most major and trace elements appear unaffected by alteration processes.  
305 Prior work has suggested that  $^{187}\text{Os}/^{188}\text{Os}$  (e.g., Snow & Reisberg, 1995; Standish et al., 2002), Re  
306 and Pd (e.g., Luguët et al., 2003; Harvey et al., 2006) can be modified by serpentinization and  
307 seafloor alteration processes but that, in general, abyssal peridotite HSE abundances are typically  
308 not strongly affected by such processes (e.g., Liu et al., 2009; Day et al., 2017a). In agreement  
309 with those studies, we find no correlation with LOI and HSE contents and Os isotopic

310 compositions (Figure S3). Indeed, it has been shown that even strongly steatized serpentinite rocks  
311 faithfully preserve original HSE abundances (Day et al., 2017b). Overall, we conclude that the  
312 bulk rock abyssal peridotite HSE compositions predominantly reflect their high temperature  
313 mantle petrogenesis.

314

315 Melt refertilization in abyssal peridotites (Niu, 2004; Seyler et al., 2004; Warren et al.,  
316 2009; Warren, 2016) can also lead to precipitation of metasomatic sulphides rich in Pd and the  
317 other HSE (Alard et al., 2000; Luguet et al., 2003). Evidence for melt refertilization in the sample  
318 suite is provided by the enrichments of non-fluid mobile highly incompatible elements in all  
319 samples (Figure 3). Enrichments of two or three orders of magnitude in the high field strength  
320 elements (HFSE: Nb, Ta, Ti, Zr, Hf) relative to what would be expected for partial melting residues  
321 are strong indicators of melt refertilization in Pacific abyssal peridotites (Figure 3), along with  
322 some LREE-enriched peridotites, as observed in slower-spreading ridges (Niu et al., 2004; Warren,  
323 2016; Day et al., 2017a). This melt infiltration has been variable between the sample suites, with  
324 plagioclase-rich melt infiltration possible in some sample suites (e.g., Hess Deep). These  
325 observations match with hand-specimen observations for AII125-6-4D-18, which include minor  
326 melt infiltration veins that are cross-cut by serpentine. Moreover, spinel grains in the Pacific  
327 abyssal peridotites plot within the lower part of the abyssal peridotite field, with relatively low Cr#  
328 at a given Mg#, which is often associated with the presence of pyroxenite-veins in the samples  
329 (e.g., Warren, 2016).

330

331 Melt infiltration events appear to have limited impact on Pt, Ru, Ir or Os abundances or Os  
332 isotopes in Pacific abyssal peridotites. In contrast, samples display variable Re contents, and Pd

333 contents to a lesser extent (Figure 4), which may be attributed to various degrees of refertilization  
334 by melts. As shown previously, basaltic melts typically have more radiogenic  $^{187}\text{Os}/^{188}\text{Os}$ , but  
335 substantially lower Os contents than peridotites, meaning that only high degrees of melt-rock  
336 reaction will lead to modification of peridotite HSE compositions (Day et al., 2017a). The  
337 generally high Os contents of the samples (~2-9 ppb) means that melt refertilization would only  
338 be notable at melt-rock ratios in excess of ten, which is not consistent with immobile incompatible  
339 trace element addition in all samples and suggests melt-rock ratios less than one. Even the  
340 peridotite with the lowest Os content in the sample set (CIRCE97-HD-2; 0.19 ppb Os) has  
341  $^{187}\text{Os}/^{188}\text{Os}$  within the range of the other peridotites, and distinct from more radiogenic MORB  
342 melts (e.g., Gannoun et al., 2016). These lines of evidence suggest that sulfide melt addition is not  
343 a significant driver in Pt, Ru, Ir or Os abundances or  $^{187}\text{Os}/^{188}\text{Os}$  in the studied abyssal peridotites.  
344 Conversely, melt refertilization can be pervasive and variable in extent from ultraslow to fast  
345 spreading ridges in modifying Re and Pd abundances (up to a factor 10 for Re abundances; Figure  
346 4).

347

#### 348 ***4.2 Recent versus ancient processes acting on abyssal peridotites***

349 Melt depletion processes can fundamentally modify peridotite compositions (e.g., Becker et  
350 al., 2006; Reisberg, 2021). It is possible to estimate the degree of melt depletion experienced by  
351 peridotites using a range of methods. For example, non-modal fractional melting models can be  
352 used to estimate melt depletion in abyssal peridotites based on REE abundances (here using model  
353 parameters outlined in Day et al., 2017a). An increase in melt depletion is associated with lower  
354 absolute REE abundances and higher depletion in the LREE relative to the HREE. The REE  
355 modeling calculations suggest 3-20% melt extraction for the WEST03MV-12 peridotites, 8-13%



356 for the WEST03MV-13 peridotites, and 15-20% for the EPR peridotites. These estimates are  
357 consistent to slightly higher than calculations of melt depletion using Cr# in spinel grains from the  
358 same samples (e.g., Batanova et al., 1998; Hellebrand et al., 2001): 13.7-19.0%, 9.6-12.3% and  
359 18.4-19.5% respectively (Table S4). The more BSE-like HSE patterns in the WEST03MV-13  
360 peridotites relate to more limited melt depletions than in other abyssal peridotite samples from the  
361 PAR and Hess Deep. The estimated high degrees of melt loss in some of the peridotites  
362 (WEST03MV-12 and Hess Deep) are consistent with clinopyroxene being nearly consumed within  
363 the mineral assemblage (Ol + Opx + Cpx + Sp) during partial melting. Correspondingly, melt  
364 extraction at fast-spreading ridges ranges up to higher values than those calculated for slow and  
365 ultraslow-spreading ridges (e.g., Warren, 2016; Day et al., 2017a) (Figure S4).

366

367 Melt extraction in the mantle typically leads to the formation of residual peridotites depleted  
368 in Re, Pd  $\pm$  Pt, relative to Ru, Ir and Os, reflecting the extraction of sulfide melt along with silicate  
369 melt, or dissolution of sulfides into the melt and formation of refractory platinum group minerals  
370 (e.g., Alard et al., 2000; Luguet et al., 2003; Ballhaus et al., 2006; Liu et al., 2009; Reisberg, 2021).  
371 Notably, Pacific abyssal peridotites tend to have BSE-like to fractionated HSE patterns with  
372 relative depletion in Re, Pd and Pt: all Pacific abyssal peridotites show similar ranges for (Pd/Ir)<sub>n</sub>  
373 and (Pt/Ir)<sub>n</sub> (WEST03MV-12 dredge: 0.5- 1.2 and 0.6 – 0.9; WEST03MV-13 dredge: 0.5-1.6 and  
374 0.5-1.0; EPR: 0.9-1.8 and 0.6-1.6 respectively). Pacific Antarctic Ridge samples with low degrees  
375 of melt depletion (WEST03MV-13) have BSE-like HSE patterns with variable rhenium depletion,  
376 whereas samples with higher degrees of melt depletion (WEST03MV-12) have more variable Re,  
377 Pd and Pt abundances (Figure 4). Two of the Hess Deep samples have patterns that are akin to  
378 BSE, while the other samples show different degrees of rhenium depletion, suggesting that, in all

379 cases, melt depletion has modified the original HSE abundances. The average total HSE content  
380 decreases with decreasing melt depletion degree (Figure S5), suggesting that the variability  
381 observed between the different ocean basins in term of HSE abundances can be explained by  
382 petrogenetic processes.

383

384 Melt depletion in peridotites decreases the incompatible element abundances. Positive  
385 correlations exist between  $\text{Al}_2\text{O}_3$ , as well as the HREE and Y, and  $^{187}\text{Os}/^{188}\text{Os}$  for the Pacific  
386 abyssal peridotites (Figure 6), as observed for peridotites from slower spreading ridges (e.g.,  
387 Reisberg and Lorand, 1995; Parkinson et al., 1998; Lassiter et al., 2014; Day et al., 2017a). Positive  
388 relationships also exist between  $\text{Al}_2\text{O}_3$  and Re/Ir and Pd/Ir, but do not occur for Pt/Ir, Ru/Ir or  
389 Os/Ir, which are essentially invariant with decreasing  $\text{Al}_2\text{O}_3$  (Table 1). Rhenium and Pd  
390 abundances in abyssal peridotites are depleted during melt loss, whereas Pt, Ru, Ir and Os  
391 abundances and  $^{187}\text{Os}/^{188}\text{Os}$  are less affected by such processes. Consequently, these correlations  
392 reflect variable melt loss in the peridotite suite. The, correlation between  $^{187}\text{Os}/^{188}\text{Os}$  and  $\text{Al}_2\text{O}_3$   
393 contents in bulk rock abyssal peridotites further implies that some of this melt depletion is also  
394 ancient, as  $^{187}\text{Os}/^{188}\text{Os}$  in these rocks tracks long-term melt depletion, where rocks with low  $\text{Al}_2\text{O}_3$   
395 also have low  $^{187}\text{Re}/^{188}\text{Os}$ . Pre-existing heterogeneities in peridotites have been noted in previous  
396  $^{187}\text{Re}$ - $^{187}\text{Os}$  studies, reporting Re depletion ages ( $T_{\text{RD}} = 1/1.67 \times 10^{-11} \times \ln\{[(0.127 -$   
397  $^{187}\text{Os}/^{188}\text{Os}_{\text{sample}})/0.40186]+1\}$ ; where  $T_{\text{RD}}$  ages represent minimum depletion ages, assuming no  
398 ingrowth from  $^{187}\text{Re}$  in abyssal peridotites since melt depletion) as ancient as 2 Ga for abyssal  
399 peridotites (e.g., Harvey et al., 2006; Liu et al., 2008; Lassiter et al., 2014; Day et al., 2017a), as  
400 well as for ophiolite peridotites (e.g., Büchl et al., 2004; Schulte et al., 2009; O'Driscoll et al.,  
401 2012, 2015) and mantle peridotites from ocean islands (Snortum et al., 2019). In this respect, it is

402 notable that the concept of the  $T_{RD}$  model age was originally developed for highly refractory  
403 cratonic peridotites, where the estimated degree of melt extraction is ~30 to 50%, leading to nearly  
404 Re-free peridotitic residues (Walker et al., 1989; Luguet and Pearson, 2019; Reisberg, 2021, and  
405 references therein). Nonetheless, measured  $^{187}\text{Os}/^{188}\text{Os}$  below the BSE or even chondritic values  
406 in mantle peridotites must reflect long-term rhenium depletion.

407

408 Rhenium depletion ages for Pacific abyssal peridotites range up to 1.3 Ga for peridotites from  
409 the WEST03MV-12 dredge, up to 1.5 Ga for those from the WEST03MV-13 dredge, and up to  
410 0.9 Ga for Hess Deep (Figure 5). The oldest rhenium depletion ages are therefore in the samples  
411 with the lowest degrees of melt depletion. The average Re depletion ages are  $0.5 \pm 0.3$  Ga,  $0.6 \pm$   
412  $0.5$  Ga and  $0.7 \pm 0.2$  Ga respectively, which are similar to previous estimates from abyssal  
413 peridotites (Lassiter et al., 2014; Day et al., 2017a). The distinction between ancient melt depletion  
414 and recent melt depletion at the ridge remains one of the most challenging issues to deconvolve in  
415 abyssal peridotites. No correlations between  $^{187}\text{Os}/^{188}\text{Os}$  or  $T_{RD}$  ages with degree of partial melting  
416 (or melt depletion,  $F$ ) are observed, suggesting that separating pre-existing melt depletion from  
417 recent-ridge melt depletion cannot be directly established. Nevertheless, Pacific abyssal peridotites  
418 with low Pd/Ir also show ancient  $T_{RD}$  ages, similar to samples from slower spreading ridges (e.g.,  
419 Lassiter et al., 2014; Day et al., 2017a), indicating that abyssal peridotites preserve significant pre-  
420 existing melt depletion, up to or exceeding 2 Ga, in some cases (Figure 5).

421

### 422 ***4.3 Pacific Ocean mantle composition***

423 Collectively, Pacific abyssal peridotites have similar distributions and variations in the  
424 abundances of the HSE, as well as slightly more radiogenic  $^{187}\text{Os}/^{188}\text{Os}$ , relative to Pacific mantle

425 xenoliths (Figure 6a) (Bizimis et al., 2007; Jackson et al., 2016; Snortum et al., 2019). Mantle  
426 xenoliths preserve melt depletion ages up to 1.5 Ga in Aitutaki (Cook Islands: Snortum et al.,  
427 2019), 1.5 Ga in Savai'i, 1.8 Ga in Tubuai (Samoa and Austral Islands respectively: Jackson et al.,  
428 2016) and as ancient as 2 Ga in O'ahu (Hawaii: Bizimis et al., 2007), similar to  $T_{RD}$  ages reported  
429 for Pacific abyssal peridotites. These observations indicate that the Pacific oceanic mantle records  
430 heterogeneous melt-depletion from both ancient and more recent melt depletion events. These melt  
431 depletion events can be up to 2 Ga and, in this sense, are similar to observations from global  
432 oceanic lithosphere (e.g., Brandon et al., 2000; Harvey et al., 2006; Liu et al., 2008, 2009; Lassiter  
433 et al., 2014; Day et al., 2017a). Even though Pacific abyssal peridotites and mantle xenoliths only  
434 provide a glimpse of the Pacific oceanic plate, often at the hand-sample scale, they show evidence  
435 for significant heterogeneities at short length scales due to prior melt depletion events up to 2 Ga  
436 ago, as well as strong similarities in average HSE abundances and Os isotope compositions to  
437 abyssal peridotites from the Atlantic, Indian or Arctic Ocean basins.

438

#### 439 *4.4 Composition of the Bulk Silicate Earth deduced from abyssal peridotites*

440 Average HSE abundances and Os isotope compositions for measured abyssal peridotites from  
441 the global mid-ocean ridge system show no correlation with spreading rate (Figure 7 and S6). This  
442 observation is important because different melting processes at slow and ultraslow spreading  
443 ridges versus fast spreading ridges could conceivably yield differences in modern melt depletion  
444 recorded in abyssal peridotites, but this is not the case. The  $^{187}\text{Os}/^{188}\text{Os}$  composition of the BSE  
445 recalculated with the new Pacific abyssal peridotites is  $0.1265 \pm 0.0031$  ( $n = 230$ ), and  $0.1250 \pm$   
446  $0.0040$  for peridotites with  $> 2$  ppb Os. These values are close to those reported by Lassiter et al.  
447 (2014) for the convecting upper mantle and by Day et al. (2017a) for the depleted MORB mantle

448 (0.1245 and  $0.1247 \pm 0.0075$  respectively). Following a similar approach as Day et al. (2017a), we  
449 recalculate the average composition of the BSE using abyssal peridotites with  $\text{Al}_2\text{O}_3$  content  $> 2$   
450 wt.% from all mid-ocean ridge systems (Figure 8). We obtain  $0.34 \pm 0.38$  (1 s.d.) ppb [Re],  $4.87$   
451  $\pm 2.67$  ppb [Pd],  $7.29 \pm 1.88$  ppb [Pt],  $7.40 \pm 1.89$  ppb [Ru],  $3.84 \pm 1.12$  ppb [Ir] and  $3.36 \pm 1.09$   
452 ppb [Os] (Figure 8). Estimates for the Arctic and Indian Oceans give comparable values to those  
453 of the global ridge system estimate (Figure 8). Note that the Atlantic Ocean estimate appears  
454 slightly depleted, and the Pacific Ocean is slightly enriched in the HSE, compared with the global  
455 BSE estimate (Figure 8). These differences can be attributed to variable degrees of ancient and  
456 modern partial melting affecting the peridotites. Similar results are obtained when the data are  
457 regressed to a BSE  $\text{Al}_2\text{O}_3$  value of 4 to 4.5 wt.% (see Day et al., 2017a).

458

459 The reevaluated composition for the BSE, including the new Pacific abyssal peridotite data,  
460 does not significantly change the average estimates for the BSE previously reported for abyssal  
461 and oceanic peridotites (Becker et al., 2006; Chatterjee and Lassiter, 2016; Day et al., 2017a), or  
462 for continental peridotites (Becker et al., 2006; Chatterjee and Lassiter, 2016). Our results for  
463 Pacific abyssal peridotites confirm that the BSE estimated from abyssal peridotites does not show  
464 high Pd/Ir and Pd enrichment as reported by Becker et al. (2006), and Chatterjee and Lassiter  
465 (2016). This discrepancy between the two estimates of the BSE compositions is thought to result  
466 from Pd enrichment in the continental-derived peridotites used for the calculation due to melt-  
467 refertilization (e.g., Aulbach et al., 2016; Luguet and Reisberg, 2016; Becker and Dale, 2016).  
468 Overall, these observations lead to the idea that the BSE shows an abundance range for the most  
469 incompatible HSE (Re, Pd) that can exceed one hundred percent, but that more compatible HSE  
470 (Pt, Ru, Ir, Os) show less than 30% abundance variation. These variations can be accounted for by

471 melting processes acting on abyssal peridotites over <2 Ga.

472

#### 473 ***4.5 Implications of a relatively homogeneous convecting mantle for the HSE***

474 Abyssal peridotites from fast to intermediate spreading ridges reveal few, if any, systematic  
475 differences in the distribution and behavior of the HSE, compared with slow to ultraslow spreading  
476 ridges, despite generally higher degrees of melt depletion (Figures 7 and 8). Additionally,  
477 estimates of the  $^{187}\text{Os}/^{188}\text{Os}$  isotope composition of the BSE based on abyssal peridotites show  
478 little to no difference to oceanic mantle xenoliths (e.g., Chatterjee and Lassiter, 2016; Snortum et  
479 al., 2019) and samples from peridotite massifs (e.g., Becker et al., 2006). Taking the available  
480 global abyssal peridotite sample set and using  $\text{Al}_2\text{O}_3 > 2$  wt.%, HSE and Os isotope compositions  
481 argue in favor of present-day convecting mantle composition, with Pt, Ru, Ir and Os abundance  
482 variations at  $<\pm 30\%$  and  $^{187}\text{Os}/^{188}\text{Os}$  variations at  $\sim 6\%$  (2SD) for the global abyssal peridotite  
483 dataset. As noted previously, this variation can be accounted for by recent rather than ancient ( $>2$   
484 Ga) processes.

485

486 Compared with abyssal peridotites (e.g., Day et al., 2017a and this study), Archean mantle  
487 peridotites from West Greenland (3.8 Ga) and Western Australia (3.46 Ga) have similar broadly  
488 chondritic  $^{187}\text{Os}/^{188}\text{Os}$  compositions and Os concentrations, arguing in favor of the HSE being  
489 added to the Earth, transported and homogenized within the mantle by  $\sim 3.8$  Ga (Bennett et al.,  
490 2002; van de Löcht et al., 2018). Homogeneous Ru isotope compositions have been reported in  
491 Archean ultramafic rocks younger than 3.5 Ga (Pilbara Craton, Australia: 3.5 - 3.2 Ga; Abitibi  
492 greenstone belt, Canada: 2.7 Ga; Bushveld, South Africa: 2.05 Ga), as well as in Phanerozoic  
493 oceanic and continental mantle domains, and are undistinguishable from the modern terrestrial

494 mantle (Bermingham and Walker, 2017; Fischer-Gödde et al., 2020). These lines of evidence all  
495 support a relatively homogenized BSE in terms of HSE abundances and Os isotope ratios since at  
496 least the Archaean, where variations reflect melting processes within the mantle, rather than  
497 heterogeneities incorporated during Earth's accretion.

498

499       Based on HSE abundances, it has been proposed that ~0.5 to 0.8% of Earth's present mass  
500 was accreted after core formation, if all HSE delivered by these impacts were retained in the  
501 mantle, rather than being lost to the core or through inefficient impact retention (Becker et al.,  
502 2006; Day et al., 2016a). Consequently, late accretion impacts might have been expected to leave  
503 graininess in HSE abundances in Earth's mantle. This is because some moderate to large size  
504 impactors may not have been capable of completely remelting Earth's mantle. From a geological  
505 perspective, Eoarchean ultramafic rocks from Greenland (3.8 - 3.7 Ga), and Mesoarchean  
506 chromitites from Seqi, Greenland (minimum age of 3 Ga) exhibit  $^{100}\text{Ru}$  excess (Fischer-Gödde et  
507 al., 2020), arguing in favor of a heterogeneous delivery of the HSE to the Earth during late  
508 accretion. Similarly, evidence for grainy accretion has been suggested for other bodies, such as  
509 Vesta (Day et al., 2012). Numerical impact models also support that delivery of silicate and metal  
510 to the Earth by large planetesimals was heterogeneous, leading to projectile material being  
511 concentrated within localized domains of Earth's mantle and producing isotopic anomalies in W,  
512 Mo and Ru isotopes (Marchi et al., 2018; Maas et al., 2021).

513

514       Geochemical arguments in favor of heterogeneities imparted to the mantle during accretion  
515 include positive  $\mu^{182}\text{W}$  preserved in most Eoarchean rocks studied to date, which have been  
516 interpreted to indicate that late accreted materials were not evenly distributed in Earth's mantle,

517 and not well mixed in the BSE (Willbold et al., 2011). Such heterogeneities are not evident in the  
518 convecting mantle, with basalts from mid-ocean ridges and ocean islands measured to date lacking  
519 positive  $\mu^{182}\text{W}$  anomalies (e.g., Mundl et al., 2017). The HSE have also been argued to have been  
520 heterogeneously distributed within the early mantle from observations that Archean (3.5 – 3.2 Ga)  
521 komatiites from the Barberton greenstone belt (South Africa) and the Pilbara craton (Western  
522 Australia) apparently record depleted HSE compositions for their mantle sources relative to late  
523 Archean and younger komatiites (Maier et al., 2009). Arguments in favor of HSE heterogeneities  
524 imparted to the mantle by late accretion are not without controversy, however, where it has been  
525 argued that komatiites are not faithful recorders of mantle source compositions (Waterton et al.,  
526 2021).

527

528       Because the HSE appear to be homogeneously mixed in the present-day convecting mantle,  
529 we favor that whatever HSE input was accreted to the Earth, these heterogeneities have been  
530 relatively efficiently mixed into the mantle through convective processes. Anomalies in the HSE,  
531 including Ru, as well as Mo and W in Archean crustal rocks can be interpreted to reflect late  
532 accretion heterogeneity within the Earth that is well-recorded within isolated crustal and  
533 lithospheric fragments. For example, the mantle beneath southwest Greenland had not yet fully  
534 equilibrated with late accretion material by 3.7 Ga ago (Fischer-Gödde et al., 2020). This is  
535 consistent with the average mantle homogenization timescale of  $\sim 1.2$  Ga calculated from the  
536 combined  $^{186}\text{Os}/^{188}\text{Os}$ - $^{187}\text{Os}/^{188}\text{Os}$  isotopic and Pt/Os and Re/Os variability in peridotites (e.g.,  
537 Chatterjee and Lassiter, 2016). Other isotopic systems, such as the short lived  $^{146}\text{Sm}$ - $^{142}\text{Nd}$  system,  
538 lead to younger mantle homogenization timescales ( $\sim 0.4$  Ga) as well as a fast mantle stirring rate  
539 (e.g., Chatterjee and Lassiter, 2016; Hyung and Jacobsen, 2020).



540

541 In contrast with lithophile incompatible elements, which are sensitive to resetting by melt  
542 refertilization in peridotites, the Re-Os and Pt-Os isotope systems are less susceptible to similar  
543 petrogenetic processes. As such, the mixing timescale inferred from Os isotopes in abyssal  
544 peridotites of around 0.5-0.7 Ga is approximately consistent with timescales predicted for the  
545 whole mantle convection. Hoffman and McKenzie (1985) showed that any convecting region of  
546 the upper mantle will be well mixed on a horizontal scale of at least 2000 km in 400 Ma, or 8500  
547 km in 1.5 Ga, suggesting that large scale heterogeneities would be destroyed within Earth's  
548 lifetime. Our data support this contention. Nonetheless, elemental and isotopic anomalies that are  
549 thought to reflect mantle heterogeneities have been recorded in ocean island basalts (e.g., HSE in  
550 the Réunion cumulate xenoliths, Peters et al., 2016; W isotope anomalies in modern flood basalts:  
551 Rizo et al., 2016; and modern ocean island basalts: Mundl et al., 2017; Mundl-Petermeier et al.,  
552 2019, 2020; Peters et al., 2021). These suggest that distinct mantle domains might have been  
553 effectively isolated and preserved from the convecting upper mantle through most of the Earth's  
554 history (e.g., Allègre and Turcotte, 1985).

555

## 556 5 CONCLUSIONS

557 This global survey of abyssal peridotites from fast to intermediate spreading ridges reveals  
558 few if any systematic differences in the distribution and behavior of the HSE, compared with slow  
559 to ultraslow spreading ridges, despite variable degrees of melt depletion. Melt refertilization is  
560 pervasive and variable in extent from ultraslow to fast spreading ridges and can modify Re and Pd  
561 quite significantly. Across ocean basins and independently of spreading rates, the HSE appear  
562 relatively homogeneous in the BSE. Using abyssal peridotites with  $\text{Al}_2\text{O}_3$  content  $> 2$  wt.% from

563 all mid-ocean ridge systems, including the new Pacific abyssal peridotite data, we recalculated the  
564 average composition of the BSE of  $0.30 \pm 0.33$  ppb [Re],  $4.94 \pm 2.35$  ppb [Pd],  $7.13 \pm 2.16$  ppb  
565 [Pt],  $7.22 \pm 3.71$  ppb [Ru],  $3.79 \pm 1.84$  ppb [Ir] and  $3.77 \pm 1.45$  ppb [Os]. Variability observed  
566 between the different ocean basins, if any, can most likely be explained by partial melting  
567 processes. The variations in HSE abundances currently observed within the convecting mantle  
568 sampled by abyssal peridotites are primarily due to partial melting and melt refertilization  
569 processes over the past 2 Ga rather than to significant HSE heterogeneity of the post-Archean  
570 mantle. Preservation of ancient melt depletion heterogeneities in some oceanic peridotites, with  
571 osmium  $T_{RD}$  ages exceeding 1 Ga and highly depleted Hf isotope signatures measured in  
572 clinopyroxene grains (Stracke et al., 2011; Sanfilippo et al., 2019) suggests some refractory  
573 domains formed through ancient melt depletion can also be partially preserved in the convecting  
574 upper mantle.

575

## 576 **ACKNOWLEDGMENTS**

577 This work was largely supported by a University of California San Diego Academic Senate Award,  
578 and in part, by the NSF Petrology and Geochemistry program (NSF EAR 1447130 and EAR  
579 1918322 to JMDD). We are grateful to Alex Hangsterfer (SIO Geological Collections) for  
580 assistance with sample curation. Dean Poeppe and Garrett Stewart are thanked for assistance with  
581 sample preparation. Constructive comments from David van Acken, the Associate Editor, Andreas  
582 Stracke, and two anonymous reviewers are gratefully acknowledged.

583

## 584 REFERENCES CITED

- 585 Alard, O., Luguet, A., Pearson, N. J., Griffin, W. L., Lorand, J. P., Gannoun, A., ... & O'Reilly, S.  
586 Y. (2005). In situ Os isotopes in abyssal peridotites bridge the isotopic gap between  
587 MORBs and their source mantle. *Nature*, 436(7053), 1005-1008.
- 588 Alard, O., Griffin, W. L., Lorand, J. P., Jackson, S. E., & O'Reilly, S. Y., 2000. Non-chondritic  
589 distribution of the highly siderophile elements in mantle sulphides. *Nature*, 407, 891-894.
- 590 Allègre, C. J., & Turcotte, D. L., 1985. Geodynamic mixing in the mesosphere boundary layer and  
591 the origin of oceanic islands. *Geophysical Research Letters*, 12(4), 207-210.
- 592 Aulbach, S., Mungall, J. E., & Pearson, D. G. (2016). Distribution and processing of highly  
593 siderophile elements in cratonic mantle lithosphere. *Reviews in Mineralogy and  
594 Geochemistry*, 81(1), 239-304.
- 595 Bach, W., Garrido, C. J., Paulick, H., Harvey, J., & Rosner, M. (2004). Seawater-peridotite  
596 interactions: First insights from ODP Leg 209, MAR 15°N. *Geochemistry, Geophysics,  
597 Geosystems*, 5(9).
- 598 Ballhaus, C., Bockrath, C., Wohlgemuth-Ueberwasser, C., Laurenz, V., & Berndt, J. (2006).  
599 Fractionation of the noble metals by physical processes. *Contributions to Mineralogy and  
600 Petrology*, 152(6), 667-684.
- 601 Batanova, V. G., Suhr, G., & Sobolev, A. V. (1998). Origin of geochemical heterogeneity in the  
602 mantle peridotites from the Bay of Islands ophiolite, Newfoundland, Canada: ion probe  
603 study of clinopyroxenes. *Geochimica et Cosmochimica Acta*, 62(5), 853-866.
- 604 Becker, H., & Dale, C. W. (2016). Re–Pt–Os isotopic and highly siderophile element behavior in  
605 oceanic and continental mantle tectonites. *Reviews in Mineralogy and  
606 Geochemistry*, 81(1), 369-440.
- 607 Becker, H., Horan, M. F., Walker, R. J., Gao, S., Lorand, J. P., & Rudnick, R. L. (2006). Highly  
608 siderophile element composition of the Earth's primitive upper mantle: constraints from  
609 new data on peridotite massifs and xenoliths. *Geochimica et Cosmochimica Acta*, 70(17),  
610 4528-4550.
- 611 Bennett, V. C., Nutman, A. P., & Esat, T. M. (2002). Constraints on mantle evolution from  
612 <sup>187</sup>Os/<sup>188</sup>Os isotopic compositions of Archean ultramafic rocks from southern West  
613 Greenland (3.8 Ga) and Western Australia (3.46 Ga). *Geochimica et Cosmochimica  
614 Acta*, 66(14), 2615-2630.
- 615 Birck, J. L., Barman, M. R., & Capmas, F. (1997). Re-Os isotopic measurements at the femtomole  
616 level in natural samples. *Geostandards newsletter*, 21(1), 19-27.
- 617 Bermingham, K. R., & Walker, R. J. (2017). The ruthenium isotopic composition of the oceanic  
618 mantle. *Earth and planetary science letters*, 474, 466-473.
- 619 Bizimis, M., Griselin, M., Lassiter, J. C., Salters, V. J., & Sen, G. (2007). Ancient recycled mantle  
620 lithosphere in the Hawaiian plume: osmium–hafnium isotopic evidence from peridotite  
621 mantle xenoliths. *Earth and Planetary Science Letters*, 257(1-2), 259-273.
- 622 Bottke, W. F., Walker, R. J., Day, J. M., Nesvorny, D., & Elkins-Tanton, L. (2010). Stochastic late  
623 accretion to Earth, the Moon, and Mars. *Science*, 330(6010), 1527-1530.

- 624 Brandon, A.D., Snow, J.E., Walker, R.J., Morgan, J.W., Mock, T.D. (2000)  $^{190}\text{Pt}$ - $^{186}\text{Os}$  and  $^{187}\text{Re}$ -  
625  $^{187}\text{Os}$  systematics of abyssal peridotites. *Earth and Planetary Science Letters*, 177, 319-335.
- 626 Brenan, J. M., Bennett, N. R., & Zajacz, Z. (2016). Experimental results on fractionation of the  
627 highly siderophile elements (HSE) at variable pressures and temperatures during planetary  
628 and magmatic differentiation. *Reviews in Mineralogy and Geochemistry*, 81(1), 1-87.
- 629 Brenan, J. M., & McDonough, W. F. (2009). Core formation and metal–silicate fractionation of  
630 osmium and iridium from gold. *Nature Geoscience*, 2(11), 798.
- 631 Büchl, A., Brüggmann, G., & Batanova, V. G. (2004). Formation of podiform chromitite deposits:  
632 implications from PGE abundances and Os isotopic compositions of chromites from the  
633 Troodos complex, Cyprus. *Chemical Geology*, 208(1-4), 217-232.
- 634 Castillo, P. R., Natland, J. H., Niu, Y., & Lonsdale, P. F. (1998). Sr, Nd and Pb isotopic variation  
635 along the Pacific–Antarctic rise/crest, 53–57 S: implications for the composition and  
636 dynamics of the South Pacific upper mantle. *Earth and Planetary Science Letters*, 154(1-  
637 4), 109-125.
- 638 Chatterjee, R., & Lassiter, J. C. (2016).  $^{186}\text{Os}/^{188}\text{Os}$  variations in upper mantle peridotites:  
639 Constraints on the Pt/Os ratio of primitive upper mantle, and implications for late veneer  
640 accretion and mantle mixing timescales. *Chemical Geology*, 442, 11-22.
- 641 Chou, C. L. (1978). Fractionation of siderophile elements in the Earth's upper mantle. In *Lunar  
642 and Planetary Science Conference Proceedings* (Vol. 9).
- 643 Cohen, A. S., & Waters, F. G. (1996). Separation of osmium from geological materials by solvent  
644 extraction for analysis by thermal ionisation mass spectrometry. *Analytica Chimica  
645 Acta*, 332(2-3), 269-275.
- 646 Day, J.M.D., O'Driscoll, B., Strachan, R.A., Daly, J.S. & Walker, R.J. (2017b) Identification of  
647 mantle peridotite as a possible Iapetan ophiolite sliver in south Shetland, Scottish  
648 Caledonides. *Journal of the Geological Society of London*, 174, 88-92.
- 649 Day, J.M.D., Walker, R.J., & Warren, J.M. (2017a).  $^{186}\text{Os}$ – $^{187}\text{Os}$  and highly siderophile element  
650 abundance systematics of the mantle revealed by abyssal peridotites and Os-rich  
651 alloys. *Geochimica et Cosmochimica Acta*, 200, 232-254.
- 652 Day, J.M.D., Waters, C.L., Schaefer, B.F., Walker, R.J., & Turner, S. (2016b). Use of hydrofluoric  
653 acid desilicification in the determination of highly siderophile element abundances and Re-  
654 Pt-Os isotope systematics in mafic-ultramafic rocks. *Geostandards and Geoanalytical  
655 Research*, 40(1), 49-65.
- 656 Day, J.M.D., Brandon, A.D., & Walker, R.J. (2016a). Highly siderophile elements in Earth, Mars,  
657 the Moon, and asteroids. *Reviews in Mineralogy and Geochemistry*, 81(1), 161-238.
- 658 Day, J.M.D., Peters, B.J., & Janney, P.E. (2014). Oxygen isotope systematics of South African  
659 olivine melilitites and implications for HIMU mantle reservoirs. *Lithos*, 202, 76-84.
- 660 Day, J.M.D., Walker, R.J., Qin, L. and Rumble III, D., 2012. Late accretion as a natural  
661 consequence of planetary growth. *Nature Geoscience*, 5(9), 614-617.
- 662 DeMets, C., Gordon, R. G., Argus, D. F., & Stein, S. (1990). Current plate motions. *Geophysical  
663 journal international*, 101(2), 425-478.

- 664 Ertel, W., O'Neill, H. S. C., Sylvester, P. J., Dingwell, D. B., & Spettel, B. (2001). The solubility  
665 of rhenium in silicate melts: implications for the geochemical properties of rhenium at high  
666 temperatures. *Geochimica et Cosmochimica Acta*, 65(13), 2161-2170.
- 667 Fischer-Gödde, M., Elfers, B. M., Münker, C., Szilas, K., Maier, W. D., Messling, N., Morishita,  
668 T., Van Kranendonk, M. & Smithies, H. (2020). Ruthenium isotope vestige of Earth's pre-  
669 late-veener mantle preserved in Archaean rocks. *Nature*, 579(7798), 240-244.
- 670 Fischer-Gödde, M., Becker, H., & Wombacher, F. (2011). Rhodium, gold and other highly  
671 siderophile elements in orogenic peridotites and peridotite xenoliths. *Chemical*  
672 *Geology*, 280(3-4), 365-383.
- 673 Frisby, C., Bizimis, M., & Mallick, S. (2016). Seawater-derived rare earth element addition to  
674 abyssal peridotites during serpentinization. *Lithos*, 248, 432-454.
- 675 Gale, A., Dalton, C. A., Langmuir, C. H., Su, Y., & Schilling, J. G. (2013). The mean composition  
676 of ocean ridge basalts. *Geochemistry, Geophysics, Geosystems*, 14(3), 489-518.
- 677 Gannoun, A., Burton, K.W., Day, J.M.D., Harvey, J., Schiano, P. & Parkinson, I. (2016). Highly  
678 siderophile element and Os Isotope Systematics of volcanic rocks at divergent and  
679 convergent plate boundaries and in intraplate settings. *Reviews in Mineralogy and*  
680 *Geochemistry*, 81, 651-724.
- 681 Haller, M. B., O'Driscoll, B., Day, J.M.D., Daly, J. S., Piccoli, P. M., & Walker, R. J. (2021).  
682 Meter-Scale Chemical and Isotopic Heterogeneities in the Oceanic Mantle, Leka Ophiolite  
683 Complex, Norway. *Journal of Petrology*, in press.  
684 <https://doi.org/10.1093/petrology/egab061>
- 685 Harvey, J., Gannoun, A., Burton, K. W., Rogers, N. W., Alard, O., & Parkinson, I. J. (2006).  
686 Ancient melt extraction from the oceanic upper mantle revealed by Re–Os isotopes in  
687 abyssal peridotites from the Mid-Atlantic ridge. *Earth and Planetary Science*  
688 *Letters*, 244(3-4), 606-621.
- 689 Hellebrand, E., Snow, J. E., Dick, H. J., & Hofmann, A. W. (2001). Coupled major and trace  
690 elements as indicators of the extent of melting in mid-ocean-ridge  
691 peridotites. *Nature*, 410(6829), 677-681.
- 692 Hoffman, N. R. A., & McKenzie, D. P. (1985). The destruction of geochemical heterogeneities by  
693 differential fluid motions during mantle convection. *Geophysical Journal*  
694 *International*, 82(2), 163-206.
- 695 Holzheid, A., Sylvester, P., O'Neill, H. S. C., Rubie, D. C., & Palme, H. (2000). Evidence for a  
696 late chondritic veneer in the Earth's mantle from high-pressure partitioning of palladium  
697 and platinum. *Nature*, 406(6794), 396-399.
- 698 Hyung, E., & Jacobsen, S. B. (2020). The  $^{142}\text{Nd}/^{144}\text{Nd}$  variations in mantle-derived rocks provide  
699 constraints on the stirring rate of the mantle from the Hadean to the present. *Proceedings*  
700 *of the National Academy of Sciences*, 117(26), 14738-14744.
- 701 Jackson, M. G., Shirey, S. B., Hauri, E. H., Kurz, M. D., & Rizo, H. (2016). Peridotite xenoliths  
702 from the Polynesian Austral and Samoa hotspots: Implications for the destruction of  
703 ancient  $^{187}\text{Os}$  and  $^{142}\text{Nd}$  isotopic domains and the preservation of Hadean  $^{129}\text{Xe}$  in the  
704 modern convecting mantle. *Geochimica et Cosmochimica Acta*, 185, 21-43.

- 705 Jagoutz, E., Palme, H., Baddenhausen, H., Blum, K., Cendales, M., Dreibus, G., Spettel, B.,  
706 Lorenz, V. & Wänke, H. (1979). The abundances of major, minor and trace elements in  
707 the earth's mantle as derived from primitive ultramafic nodules. In *Lunar and Planetary*  
708 *Science Conference Proceedings* (Vol. 10, pp. 2031-2050).
- 709 Jones, J. H., & Drake, M. J. (1986). Geochemical constraints on core formation in the  
710 Earth. *Nature*, 322(6076), 221-228.
- 711 Kimura, K. A. N., Lewis, R. S., & Anders, E. (1974). Distribution of gold and rhenium between  
712 nickel-iron and silicate melts: implications for the abundance of siderophile elements on  
713 the Earth and Moon. *Geochimica et Cosmochimica Acta*, 38(5), 683-701.
- 714 Klein, F., Bach, W., & McCollom, T. M. (2013). Compositional controls on hydrogen generation  
715 during serpentinization of ultramafic rocks. *Lithos*, 178, 55-69.
- 716 Lassiter, J. C., Byerly, B. L., Snow, J. E., & Hellebrand, E. (2014). Constraints from Os-isotope  
717 variations on the origin of Lena Trough abyssal peridotites and implications for the  
718 composition and evolution of the depleted upper mantle. *Earth and Planetary Science*  
719 *Letters*, 403, 178-187.
- 720 Liu, C. Z., Snow, J. E., Brüggmann, G., Hellebrand, E., & Hofmann, A. W. (2009). Non-chondritic  
721 HSE budget in Earth's upper mantle evidenced by abyssal peridotites from Gakkel ridge  
722 (Arctic Ocean). *Earth and Planetary Science Letters*, 283(1-4), 122-132.
- 723 Liu, C. Z., Snow, J. E., Hellebrand, E., Brüggmann, G., Von Der Handt, A., Büchl, A., & Hofmann,  
724 A. W. (2008). Ancient, highly heterogeneous mantle beneath Gakkel ridge, Arctic  
725 Ocean. *Nature*, 452(7185), 311-316.
- 726 Lorand, J. P., & Luguet, A. (2016). Chalcophile and siderophile elements in mantle rocks: Trace  
727 elements controlled by trace minerals. *Reviews in Mineralogy and Geochemistry*, 81(1),  
728 441-488.
- 729 Luguet, A., & Pearson, G. (2019). Dating mantle peridotites using Re-Os isotopes: The complex  
730 message from whole rocks, base metal sulfides, and platinum group minerals. *American*  
731 *Mineralogist: Journal of Earth and Planetary Materials*, 104(2), 165-189.
- 732 Luguet, A., & Reisberg, L. (2016). Highly siderophile element and 187Os signatures in non-  
733 cratonic basalt-hosted peridotite xenoliths: Unravelling the origin and evolution of the post-  
734 Archean lithospheric mantle. *Reviews in Mineralogy and Geochemistry*, 81(1), 305-367.
- 735 Luguet, A., Lorand, J. P., & Seyler, M. (2003). Sulfide petrology and highly siderophile element  
736 geochemistry of abyssal peridotites: A coupled study of samples from the Kane Fracture  
737 Zone (45°W 23°20N, MARK area, Atlantic Ocean). *Geochimica et Cosmochimica*  
738 *Acta*, 67(8), 1553-1570.
- 739 Luguet, A., Alard, O., Lorand, J. P., Pearson, N. J., Ryan, C., & O'Reilly, S. Y. (2001). Laser-  
740 ablation microprobe (LAM)-ICPMS unravels the highly siderophile element geochemistry  
741 of the oceanic mantle. *Earth and Planetary Science Letters*, 189(3-4), 285-294.
- 742 Maas, C., Manske, L., Wünnemann, K., & Hansen, U. (2021). On the fate of impact-delivered  
743 metal in a terrestrial magma ocean. *Earth and Planetary Science Letters*, 554, 116680.

- 744 Maier, W.D., Barnes, S.J., Campbell, I.H., Fiorentini, M.L., Peltonen, P., Barnes, S.J. and  
745 Smithies, R.H., 2009. Progressive mixing of meteoritic veneer into the early Earth's deep  
746 mantle. *Nature*, 460(7255), pp.620-623
- 747 Malvoisin, B. (2015). Mass transfer in the oceanic lithosphere: serpentinization is not  
748 isochemical. *Earth and Planetary Science Letters*, 430, 75-85.
- 749 Marchesi, C., Dale, C. W., Garrido, C. J., Pearson, D. G., Bosch, D., Bodinier, J. L., Gervilla, F.  
750 & Hidas, K. (2014). Fractionation of highly siderophile elements in refertilized mantle:  
751 Implications for the Os isotope composition of basalts. *Earth and Planetary Science*  
752 *Letters*, 400, 33-44.
- 753 Marchi, S., Canup, R.M. and Walker, R.J., 2018. Heterogeneous delivery of silicate and metal to  
754 the Earth by large planetesimals. *Nature geoscience*, 11(1), pp.77-81.
- 755 Martin, C.E. (1991) Osmium isotopic characteristics of mantle-derived rocks. *Geochimica et*  
756 *Cosmochimica Acta*, 55, 1421-1434.
- 757 Meisel, T., & Horan, M. F. (2016). Analytical methods for the highly siderophile  
758 elements. *Reviews in Mineralogy and Geochemistry*, 81(1), 89-106.
- 759 Meisel, T., Walker, R. J., & Morgan, J. W. (1996). The osmium isotopic composition of the Earth's  
760 primitive upper mantle. *Nature*, 383(6600), 517-520.
- 761 Morgan, J. W. (1986). Ultramafic xenoliths: clues to Earth's late accretionary history. *Journal of*  
762 *Geophysical Research: Solid Earth*, 91(B12), 12375-12387.
- 763 Morgan, J. W., Walker, R. J., Brandon, A. D., & Horan, M. F. (2001). Siderophile elements in  
764 Earth's upper mantle and lunar breccias: data synthesis suggests manifestations of the same  
765 late influx. *Meteoritics & Planetary Science*, 36(9), 1257-1275.
- 766 Mundl-Petermeier, A., Walker, R. J., Fischer, R. A., Lekic, V., Jackson, M. G., & Kurz, M. D.  
767 (2020). Anomalous  $^{182}\text{W}$  in high  $^3\text{He}/^4\text{He}$  ocean island basalts: Fingerprints of Earth's  
768 core? *Geochimica et Cosmochimica Acta*, 271, 194-211.
- 769 Mundl-Petermeier A., Walker R. J., Jackson M. G., Blichert-Toft J., Kurz M. D. and Halldórsson  
770 S. A. (2019) Temporal evolution of primordial tungsten-182 and  $^3\text{He}/^4\text{He}$  signatures in the  
771 Iceland mantle plume. *Chem. Geol.* 525, 245–259.
- 772 Mundl, A., Touboul, M., Jackson, M. G., Day, J.M.D., Kurz, M. D., Lekic, V., Helz, R. T. &  
773 Walker, R. J. (2017). Tungsten-182 heterogeneity in modern ocean island  
774 basalts. *Science*, 356(6333), 66-69.
- 775 Murthy, V. R. (1991). Early differentiation of the Earth and the problem of mantle siderophile  
776 elements: a new approach. *Science*, 253(5017), 303-306.
- 777 Niu, Y. (2004). Bulk-rock major and trace element compositions of abyssal peridotites:  
778 implications for mantle melting, melt extraction and post-melting processes beneath mid-  
779 ocean ridges. *Journal of Petrology*, 45(12), 2423-2458.
- 780 O'Driscoll, B., Walker, R. J., Day, J. M. D., Ash, R. D., & Daly, J. S. (2015). Generations of melt  
781 extraction, melt–rock interaction and high-temperature metasomatism preserved in  
782 peridotites of the ~497 Ma Leka Ophiolite Complex, Norway. *Journal of Petrology*, 56(9),  
783 1797-1828.

- 784 O'Driscoll, B., Day, J. M. D., Walker, R. J., Daly, J. S., McDonough, W. F., & Piccoli, P. M.  
785 (2012). Chemical heterogeneity in the upper mantle recorded by peridotites and chromitites  
786 from the Shetland Ophiolite Complex, Scotland. *Earth and Planetary Science Letters*, 333,  
787 226-237.
- 788 O'Neill, H. S. C., Dingwell, D. B., Borisov, A., Spettel, B., & Palme, H. (1995). Experimental  
789 petrochemistry of some highly siderophile elements at high temperatures, and some  
790 implications for core formation and the mantle's early history. *Chemical Geology*, 120(3-  
791 4), 255-273.
- 792 Paquet, M., Cannat, M., Brunelli, D., Hamelin, C., & Humler, E. (2016). Effect of melt/mantle  
793 interactions on MORB chemistry at the easternmost Southwest Indian Ridge (61°–67°  
794 E). *Geochemistry, Geophysics, Geosystems*, 17(11), 4605-4640.
- 795 Parkinson, I. J., Hawkesworth, C. J., & Cohen, A. S. (1998). Ancient mantle in a modern arc:  
796 Osmium isotopes in Izu-Bonin-Mariana forearc peridotites. *Science*, 281(5385), 2011-  
797 2013.
- 798 Paulick, H., Bach, W., Godard, M., De Hoog, J. C. M., Suhr, G., & Harvey, J. (2006).  
799 Geochemistry of abyssal peridotites (Mid-Atlantic Ridge, 15 20' N, ODP Leg 209):  
800 implications for fluid/rock interaction in slow spreading environments. *Chemical*  
801 *Geology*, 234(3-4), 179-210.
- 802 Peters, B. J., Mundl-Petermeier, A., Carlson, R. W., Walker, R. J., & Day, J. M. (2021). Combined  
803 Lithophile-Siderophile Isotopic Constraints on Hadean Processes Preserved in Ocean  
804 Island Basalt Sources. *Geochemistry, Geophysics, Geosystems*, 22(3), e2020GC009479.
- 805 Peters, B. J., Day, J.M.D., & Taylor, L. A. (2016). Early mantle heterogeneities in the Réunion  
806 hotspot source inferred from highly siderophile elements in cumulate xenoliths. *Earth and*  
807 *Planetary Science Letters*, 448, 150-160.
- 808 Rehkämper, M., Halliday, A. N., Fitton, J. G., Lee, D. C., Wieneke, M., & Arndt, N. T. (1999). Ir,  
809 Ru, Pt, and Pd in basalts and komatiites: new constraints for the geochemical behavior of  
810 the platinum-group elements in the mantle. *Geochimica et Cosmochimica Acta*, 63(22),  
811 3915-3934.
- 812 Reisberg, L. (2021). Osmium isotope constraints on formation and refertilization of the non-  
813 cratonic continental mantle lithosphere. *Chemical Geology*, 574, 120245.
- 814 Reisberg, L., & Lorand, J. P. (1995). Longevity of sub-continental mantle lithosphere from  
815 osmium isotope systematics in orogenic peridotite massifs. *Nature*, 376(6536), 159-162.
- 816 Ringwood, A. E. (1977). Composition of the core and implications for origin of the  
817 Earth. *Geochemical Journal*, 11(3), 111-135.
- 818 Rizo, H., Walker, R. J., Carlson, R. W., Horan, M. F., Mukhopadhyay, S., Manthos, V., ... &  
819 Jackson, M. G. (2016). Preservation of Earth-forming events in the tungsten isotopic  
820 composition of modern flood basalts. *Science*, 352(6287), 809-812.
- 821 Rouméjon, S. (2014). Serpentinisation des péridotites exhumées aux dorsales lentes : approches  
822 microstructurale, minéralogique et géochimique. *Institut de Physique du Globe de Paris*.
- 823 Roy-Barman, M., & Allègre, C. J. (1994).  $^{187}\text{Os}/^{186}\text{Os}$  ratios of mid-ocean ridge basalts and abyssal  
824 peridotites. *Geochimica et Cosmochimica Acta*, 58(22), 5043-5054.



- 825 Sanfilippo, A., Salters, V., Tribuzio, R., & Zanetti, A. (2019). Role of ancient, ultra-depleted  
826 mantle in Mid-Ocean-Ridge magmatism. *Earth and Planetary Science Letters*, 511, 89-98.
- 827 Schulte, R. F., Schilling, M., Anma, R., Farquhar, J., Horan, M. F., Komiya, T., Farquhar, J.,  
828 Piccoli, P. M., Pitcher, L. & Walker, R. J. (2009). Chemical and chronologic complexity  
829 in the convecting upper mantle: Evidence from the Taitao ophiolite, southern  
830 Chile. *Geochimica et Cosmochimica Acta*, 73(19), 5793-5819.
- 831 Seyler, M., Lorand, J. P., Toplis, M. J., & Godard, G. (2004). Asthenospheric metasomatism  
832 beneath the mid-ocean ridge: Evidence from depleted abyssal peridotites. *Geology*, 32(4),  
833 301-304.
- 834 Seyler, M., Cannat, M., & Mével, C. (2003). Evidence for major-element heterogeneity in the  
835 mantle source of abyssal peridotites from the Southwest Indian Ridge (52° to  
836 68°E). *Geochemistry, Geophysics, Geosystems*, 4(2).
- 837 Sichel, S.E., Esperanca, S., Motoki, A., Maia M., Horan, M.F., Szatmari, P., da Costa Alves, E.,  
838 Mello, S.L.M. (2008). Geophysical and geochemical evidence for cold upper mantle  
839 beneath the equatorial Atlantic Ocean. *Revista Brasileira de Geofísica*, 26, 69-86.
- 840 Snortum, E., Day, J.M.D. (2020) Forearc origin for Coast Range Ophiolites inferred from osmium  
841 isotopes and highly siderophile elements. *Chemical Geology*, 550, 119723.
- 842 Snortum, E., Day, J.M.D., & Jackson, M. G. (2019). Pacific lithosphere evolution inferred from  
843 Aitutaki mantle xenoliths. *Journal of Petrology*, 60(9), 1753-1772.
- 844 Snow, J.E., & Dick, H.J. (1995). Pervasive magnesium loss by marine weathering of  
845 peridotite. *Geochimica et Cosmochimica Acta*, 59(20), 4219-4236.
- 846 Snow, J. E., & Reisberg, L. (1995). Os isotopic systematics of the MORB mantle: results from  
847 altered abyssal peridotites. *Earth and Planetary Science Letters*, 133(3-4), 411-421.
- 848 Snow, J. E., & Schmidt, G. (1998). Constraints on Earth accretion deduced from noble metals in  
849 the oceanic mantle. *Nature*, 391(6663), 166-169.
- 850 Standish, J.J., Hart, S.R., Blusztajn, J., Dick, H.J.B., Lee, K.L. (2002) Abyssal peridotite osmium  
851 isotopic compositions from Cr-spinel. *Geochemistry, Geophysics, Geosystems*, 3,  
852 10.1029/2001GC000161.
- 853 Stracke, A., Snow, J. E., Hellebrand, E., von der Handt, A., Bourdon, B., Birbaum, K., & Günther,  
854 D. (2011). Abyssal peridotite Hf isotopes identify extreme mantle depletion. *Earth and  
855 Planetary Science Letters*, 308(3-4), 359-368.
- 856 Suer, T.-A., Siebert, J., Remusat, L., Day, J.M.D., Borensztajn, S., Doisineau, B., Fiquet, G. (2021)  
857 Reconciling metal-silicate partitioning and late accretion in the Earth. *Nature  
858 Communications*. 12, 2193. <https://doi.org/10.1038/s41467-021-23137-5>.
- 859 Turekian, K. K., & Clark Jr, S. P. (1969). Inhomogeneous accumulation of the Earth from the  
860 primitive solar nebula. *Earth and Planetary Science Letters*, 6(5), 346-348.
- 861 Van de Löcht, J., Hoffmann, J. E., Li, C., Wang, Z., Becker, H., Rosing, M. T., Münker, C. (2018).  
862 Earth's oldest mantle peridotites show entire record of late accretion. *Geology*, 46(3), 199-  
863 202.

- 864 Walker, R. J., Carlson, R. W., Shirey, S. B., & Boyd, F. R. (1989). Os, Sr, Nd, and Pb isotope  
865 systematics of southern African peridotite xenoliths: implications for the chemical  
866 evolution of subcontinental mantle. *Geochimica et Cosmochimica Acta*, 53(7), 1583-1595.
- 867 Wänke, H. (1981). Constitution of terrestrial planets. *Philosophical Transactions of the Royal*  
868 *Society of London. Series A, Mathematical and Physical Sciences*, 303(1477), 287-302.
- 869 Warren, J. M. (2016). Global variations in abyssal peridotite compositions. *Lithos*, 248, 193-219.
- 870 Warren, J. M., Shimizu, N., Sakaguchi, C., Dick, H. J. B., & Nakamura, E. (2009). An assessment  
871 of upper mantle heterogeneity based on abyssal peridotite isotopic compositions. *Journal*  
872 *of Geophysical Research: Solid Earth*, 114(B12).
- 873 Waterton, P., Mungall, J., & Pearson, D. G. (2021). The komatiite-mantle platinum-group element  
874 paradox. *Geochimica et Cosmochimica Acta*.
- 875 Willbold, M., Elliott, T., & Moorbath, S. (2011). The tungsten isotopic composition of the Earth's  
876 mantle before the terminal bombardment. *Nature*, 477(7363), 195-198.
- 877 Zhang, C., Liu, C. Z., Ji, W. B., Liu, T., & Wu, F. Y. (2020). Heterogeneous sub-ridge mantle of  
878 the Neo-Tethys: Constraints from Re-Os isotope and HSE compositions of the Xigaze  
879 ophiolites. *Lithos*, 105819.
- 880

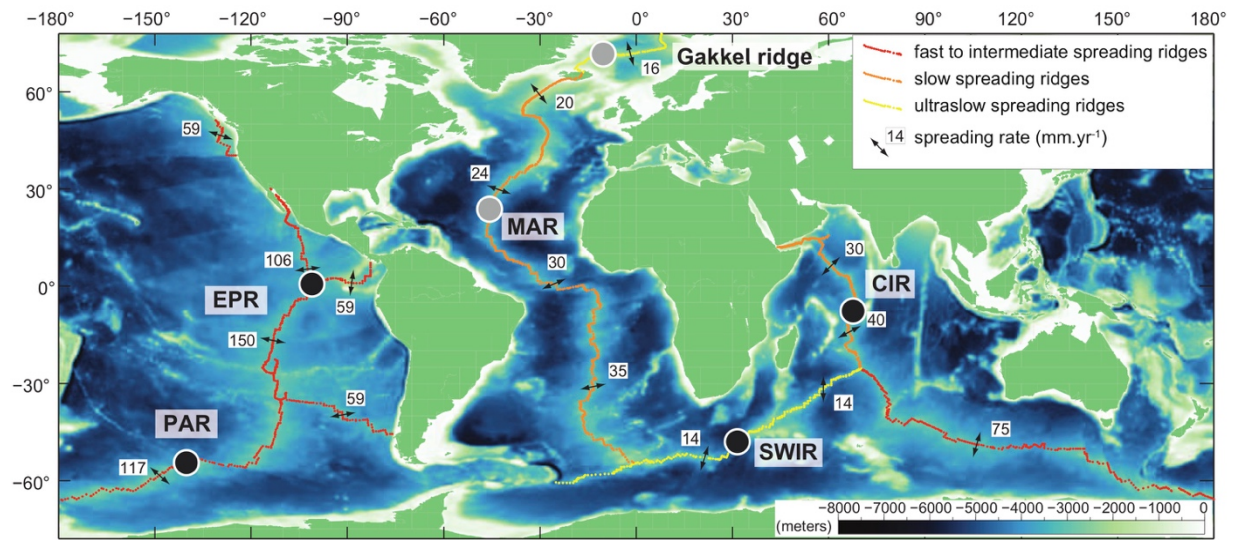
881 **TABLE CAPTIONS**

882 **Table 1.** Osmium isotope and highly siderophile element abundance (ppb) data in abyssal  
883 peridotites.

884 **Tables S1 to S7.** Ancillary, major, trace element and the available published HSE and Os isotope  
885 dataset for abyssal peridotites. Accuracy and precision for standard reference materials and total  
886 procedural blanks are provided for isotope dilution HSE abundance analyses.

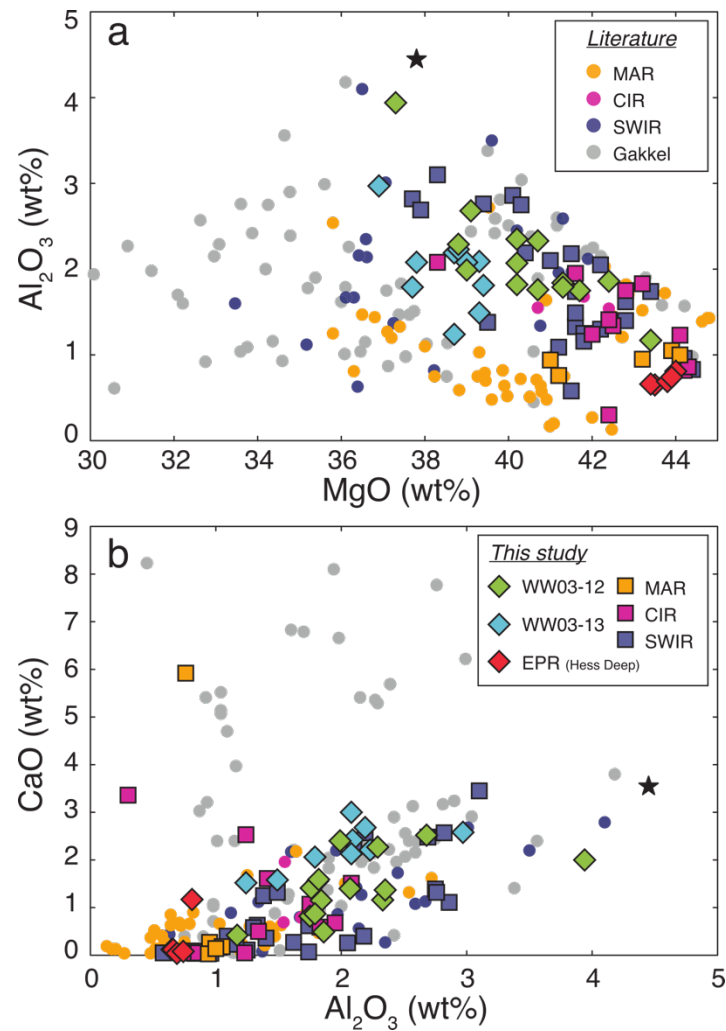
887

## 888 FIGURES &amp; FIGURE CAPTIONS



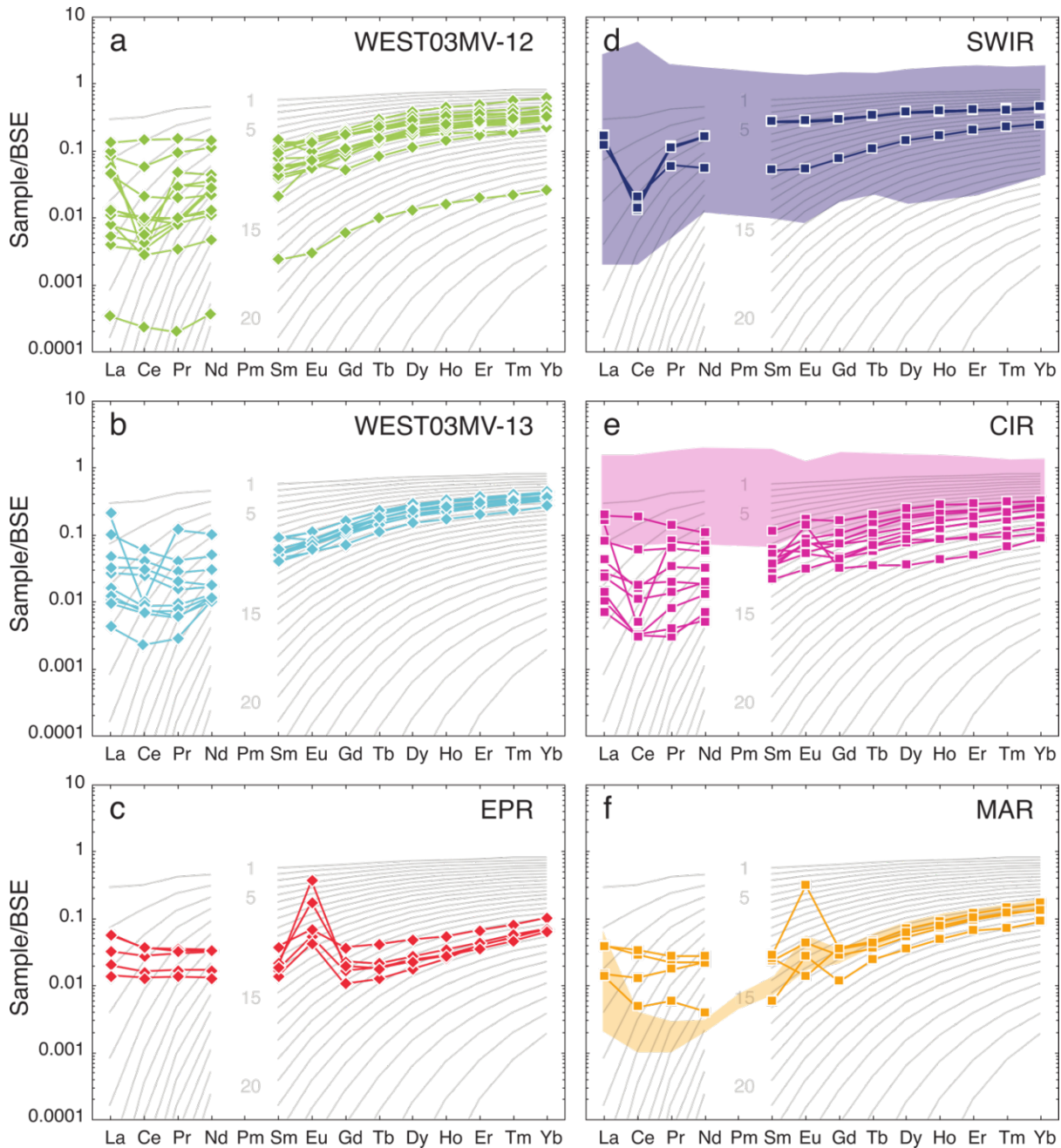
889

890 **Figure 1.** Mid-ocean ridge full spreading rates and the location of abyssal peridotites analyzed for  
 891 Re-Os isotopes and HSE abundance systematics in this study (EPR, PAR, SWIR, CIR) and prior  
 892 studies (modified from Rouméjon, 2014). Spreading rates are from DeMets et al. (1990). The black  
 893 circles represent locations of new HSE and Os isotope data for abyssal peridotites from Hess Deep  
 894 along the East Pacific Rise (EPR) and from the Udintsev fracture zone along the Pacific Antarctic  
 895 Ridge (PAR), as well as from the Central and Southwest Indian Ridges. The light gray circles  
 896 correspond to abyssal peridotite samples from other slower spreading centers (Snow and Schmidt,  
 897 1998; Brandon et al., 2000, 2006; Lugué et al., 2001, 2003; Becker et al., 2006; Liu et al., 2009;  
 898 Lassiter et al., 2014; Day et al., 2017a; Li et al., 2019).



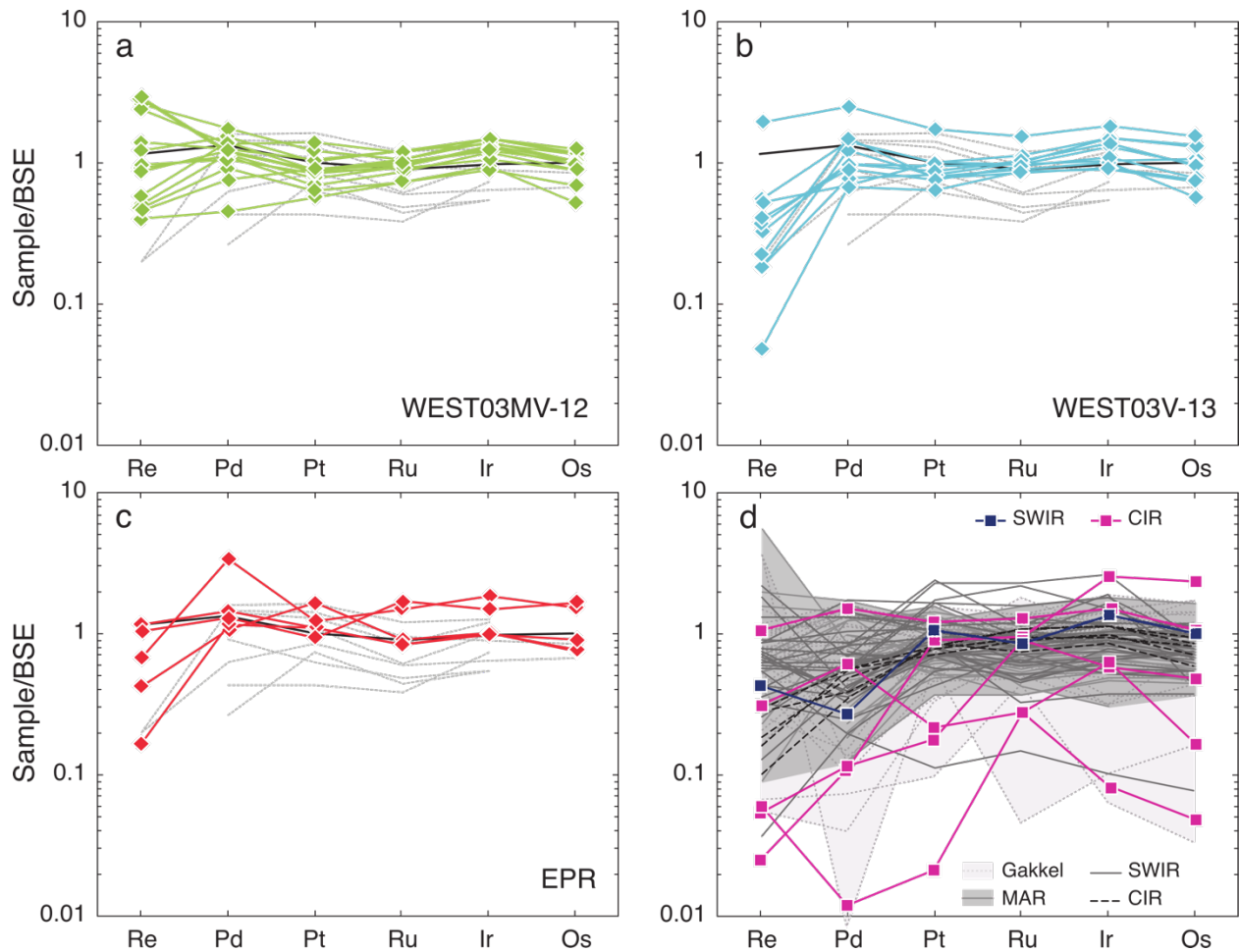
899

900 **Figure 2.** Variations (in wt.%) of (a) Al<sub>2</sub>O<sub>3</sub> as a function of MgO and (b) CaO as a function of  
 901 Al<sub>2</sub>O<sub>3</sub> for bulk rock abyssal peridotites from the dredges WEST03MV-12 and WEST03MV-13  
 902 (abbreviated WW03-12 and WW03-13 respectively) along the Pacific Antarctic Ridge, Hess Deep  
 903 region along the East Pacific Rise, the Southwest Indian Ridge, the Central Indian Ridge and the  
 904 Mid-Atlantic Ridge. Also shown for comparison are abyssal peridotites from the Gakkel ridge, the  
 905 Southwest Indian Ridge, the Central Indian Ridge and the Mid-Atlantic Ridge for which HSE and  
 906 Os isotope data are available (see Table S7 for references). The star corresponds to the Primitive  
 907 Mantle estimate from McDonough and Sun (1995). (For interpretation of the references to color  
 908 in this figure legend, the reader is referred to the web version of this article).



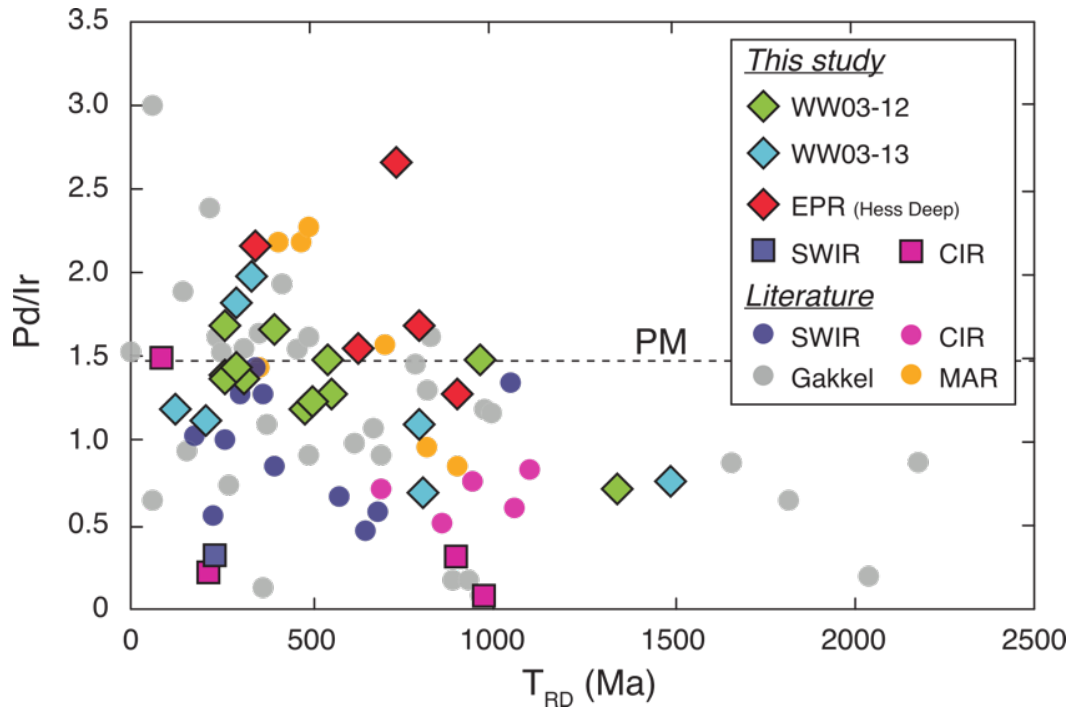
909

910 **Figure 3.** Bulk Silicate Earth-normalized rare earth element (REE) concentrations in abyssal  
 911 peridotites from the dredges WEST03MV-12 (a) and WEST03MV-13 (b) along the Pacific  
 912 Antarctic Ridge (PAR), Hess Deep region along the East Pacific Rise (EPR) (c), SWIR (d), CIR  
 913 (e) and MAR (f). Shaded fields are abyssal peridotites from Day et al., (2017a). Normalizing values  
 914 from McDonough & Sun (1995). Gray lines represent 1% melt increments for a non-modal  
 915 fractional melting model (see Day et al., 2017a for model parameters). An increase of melt  
 916 depletion is associated with lower absolute REE abundances and higher depletion in the LREE  
 917 relative to the HREE.



918

919 **Figure 4.** Bulk Silicate Earth-normalized HSE concentrations in abyssal peridotites from the  
 920 dredges WEST03MV-12 (a) and WEST03MV-13 (b) along the Pacific Antarctic Ridge (PAR),  
 921 Hess Deep region along the East Pacific Rise (EPR) (c), SWIR and CIR, together with slow-  
 922 spreading ridge abyssal peridotite literature data as comparison (Brandon et al., 2000; Liu et al.,  
 923 2009; Lassiter et al., 2014; Day et al., 2017a; Li et al., 2019) (d). Normalizing values from Day et  
 924 al. (2017a). Gray dashed lines correspond to previous studies on Hess Deep abyssal peridotites  
 925 (Snow & Schmidt, 1998; Rehkämper et al., 1999). The black solid line in panels a-c corresponds  
 926 to the Primitive Upper Mantle (PUM) estimate from Becker et al. (2006).

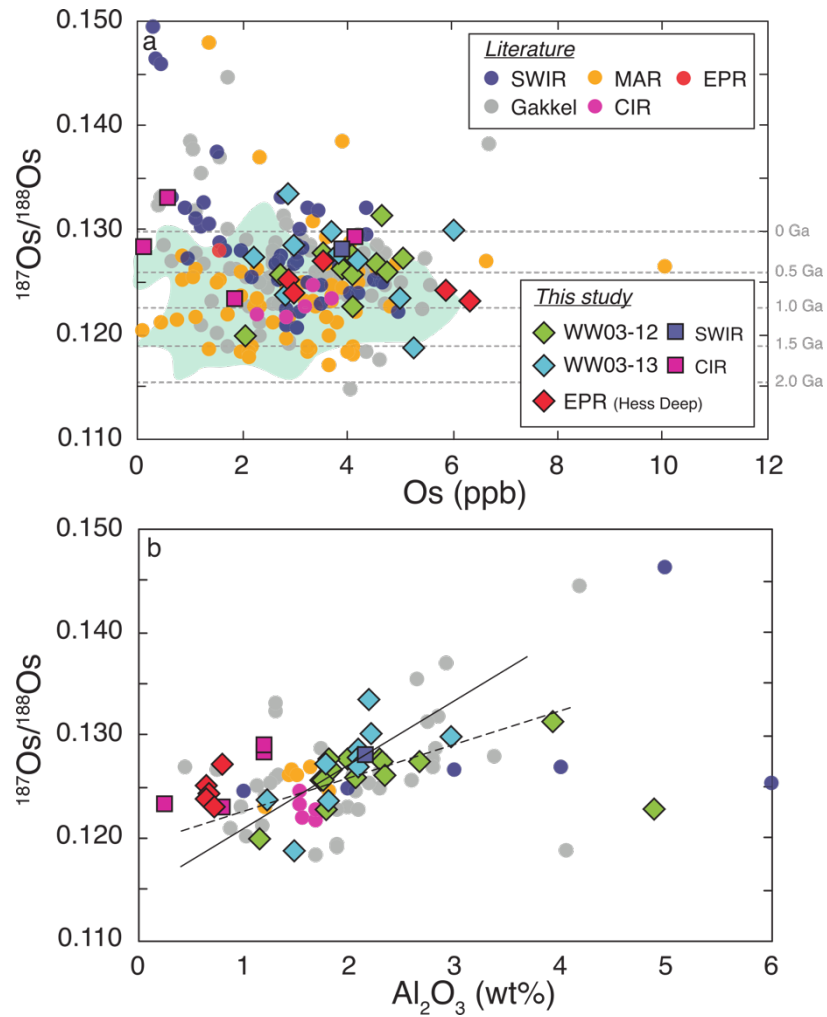


927

928 **Figure 5.** Time of Re depletion model ages ( $T_{RD}$ ) versus Pd/Ir. Primitive mantle (also referred to  
 929 as BSE) Pd/Ir is from Day et al. (2017a). Literature data are from Snow and Schmidt (1998),  
 930 Becker et al., 2006, Liu et al. (2008, 2009), and Day et al. (2017a). (For interpretation of the  
 931 references to color in this figure legend, the reader is referred to the web version of this article).

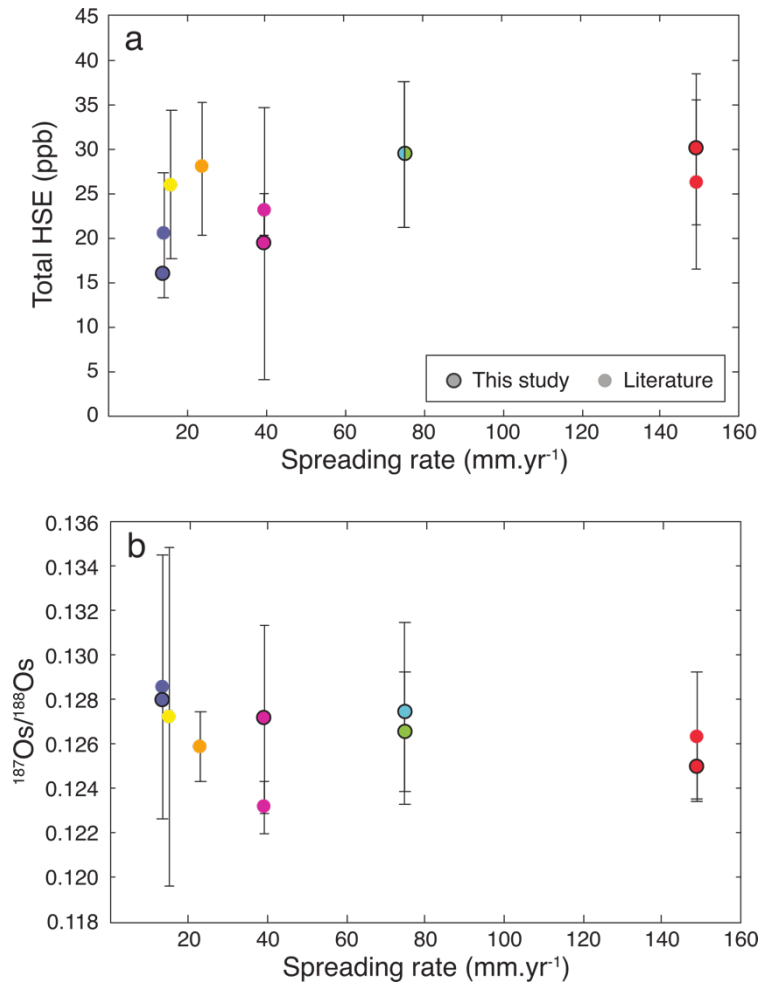


932



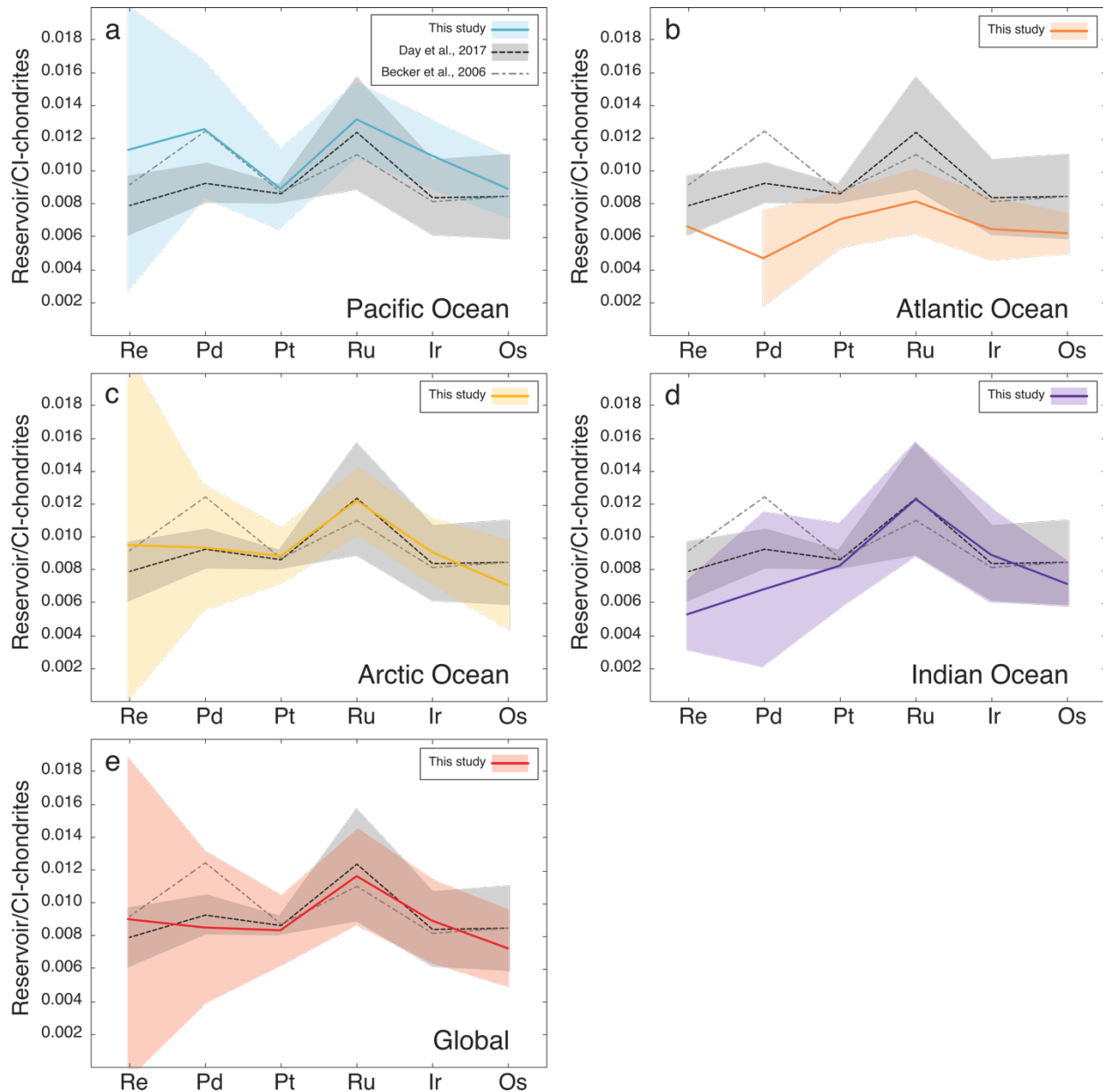
933

934 **Figure 6.** Relationship between  $^{187}\text{Os}/^{188}\text{Os}$  ratios and (a) Os and (b)  $\text{Al}_2\text{O}_3$  contents in abyssal  
 935 peridotites. The dashed and solid lines correspond to the linear regression for the WEST03MV-12  
 936 ( $r^2 = 0.64$ ) and WEST03MV-13 peridotites ( $r^2 = 0.5$ ), respectively. Literature data for abyssal  
 937 peridotites are given in the text and can be found in Supplementary Table 7. The green field  
 938 represents the peridotite xenoliths from the Pacific Ocean (Bizimis et al., 2007; Jackson et al.,  
 939 2016; Snortum et al., 2019). The dotted grey lines are the depletion ages for a BSE composition.  
 940 (For interpretation of the references to color in this figure legend, the reader is referred to the web  
 941 version of this article).



942

943 **Figure 7.** Average (a) total HSE contents in ppb, and (b)  $^{187}\text{Os}/^{188}\text{Os}$  ratios as a function of  
944 spreading rate. Spreading rates are as reported in Figure 1.



945

946 **Figure 8.** Estimates for the mantle composition for each ocean basin (solid lines), considered to  
 947 be represented by abyssal peridotites with  $\text{Al}_2\text{O}_3 > 2$  wt.% (this study; Brandon et al., 2000; Liu et  
 948 al., 2009; Lassiter et al., 2014; Day et al., 2017a; Li et al., 2019) (a) Pacific Ocean, (b) Atlantic  
 949 Ocean, (c) Arctic Ocean, (d) Indian Ocean and (e) for the global abyssal peridotite sample suite.  
 950 Colored fields correspond to the standard deviation of the calculated mantle composition. Dashed  
 951 lines correspond to the primitive (upper) mantle estimates from Becker et al., (2006) and Day et  
 952 al. (2017a). The grey field represents the 2 SD uncertainty of the estimate from Day et al. (2017a).  
 953 Note that abyssal peridotites from the CIR and Hess Deep along the EPR were not included in the  
 954 calculation for the Indian and Pacific oceans due to their low  $\text{Al}_2\text{O}_3$  content. (For interpretation of  
 955 the references to color in this figure legend, the reader is referred to the web version of this article).